

RESEARCH

Open Access



Biomimetic gold nano-modulator for deep-tumor NIR-II photothermal immunotherapy via gaseous microenvironment remodeling strategy

Honglin Huang^{1†}, Zhengxin Xie^{1†}, Ningxi Li¹, Li Zeng¹, Qianyi Zeng¹, Ziman Yang¹, Jinyang Shen¹, Hong Yang¹, Yiyao Liu^{1,2,3*} and Chunhui Wu^{1*}

Abstract

Introduction Effective immunotherapeutic treatment of solid tumors has been greatly challenged by the complex hostile tumor immunosuppressive microenvironment (TIME), which typically involves hypoxia and immunosuppression.

Methods Herein, a multifunctional biomimetic gold nano-modulator (denoted as **GNR-SNO@MMT**) was developed to realize the efficient second near-infrared (NIR-II) photothermal immunotherapy via tumor targeting and deep penetration, vascular normalization and immune reprogramming. NIR-II photothermal agent gold nanorods (GNR) were grafted with thermosensitive S-nitrosothiol (SNO) donors and camouflaged with the tumor-penetrating peptide tLyp-1-modified macrophage membrane (MM) to yield **GNR-SNO@MMT**.

Results The engineered membrane coating increased the capacity for tumor inflammatory tropism and deep penetration, which aided **GNR-SNO@MMT** in ablating tumors together with NIR-II laser irradiation. Moreover, hyperthermia-stimulated nitric oxide (NO) release in situ acted as a gas immunomodulator to effectively enhance blood perfusion and reprogram the TIME via multiple functions (e.g., decreasing PD-L1, repolarizing tumor-associated macrophages, and revitalizing cytotoxic T cells). Ultimately, the inhibition rate against 4T1 mouse mammary tumor model mediated by **GNR-SNO@MMT** plus NIR-II laser was 94.7% together with 2.4-fold CD8⁺ T cells infiltrated into tumors than that of the untreated counterpart.

Conclusions The engineered biomimetic nano-modulator of **GNR-SNO@MMT** provides an effective and novel photoimmunotherapy candidate against deep-sited solid tumors through immune reconfiguration *via* NO-involved nanomedicine and external NIR-II laser assistance.

[†]Honglin Huang and Zhengxin Xie contributed equally to this work.

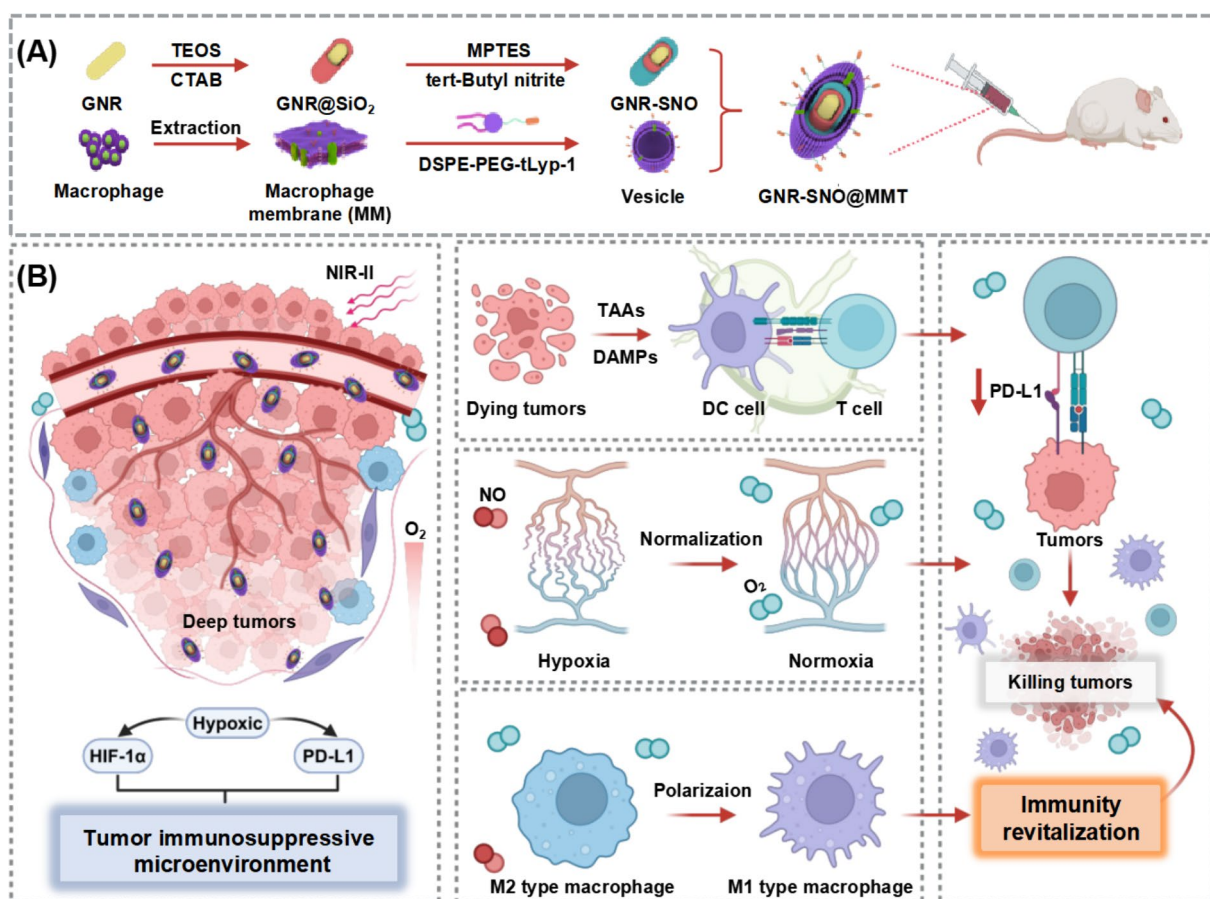
*Correspondence:

Yiyao Liu
liuyiyao@uestc.edu.cn
Chunhui Wu
wuchunhui@uestc.edu.cn

Full list of author information is available at the end of the article



Graphical abstract



Keywords NIR-II photothermal therapy, Macrophage membrane biomimetic system, Gas immunomodulator, Immunosuppression relief

Introduction

Immunotherapy, as the “third revolution” in cancer treatment, activates the patient’s own immune system to kill the primary, metastasized tumors, and reoccurred tumor cells due to its effectiveness, durability, and memory ability [1, 2]. Typically, photothermal immunotherapy stands out for the effective and precise treatment of solid tumors on the basis of the spatiotemporal control of immunogenic cell death (ICD) occurrence by an exogenous laser stimulus [3]. Multiple photothermal agents (PTAs), including organic [4–6] and inorganic agents [7, 8] have been reported to elicit effective photothermal immunotherapy against various malignant tumor modes. Compared with conventional PTAs with absorption in the first near-infrared (NIR-I, 700–900 nm) window, the NIR-II (900–1700 nm) PTAs are more preferable due to the deeper tissue penetration, less light scattering, and minimal background signals of NIR-II laser [9]. Gold nanorods (GNR) have been found to be biocompatible

and effective NIR-II PTAs because of the tuned aspect ratio with optimized NIR-II localized surface plasmon resonance (LSPR) and sufficient photothermal conversion efficiency [10–12]. Additionally, GNR can load different immune adjuvants to further amplify anticancer immunity. However, the complex environment in solid tumors greatly limits the effectiveness of nanoparticle (such as GNR)-based immunotherapy. The condensed matrix environment with broken blood vessels and interstitial fluid pressure inside solid tumors greatly prevents the access of PTAs and even the infiltration of immune cells. Moreover, the tumor immunosuppressive microenvironment (TIME) consist of tumor-associated macrophages (TAMs), myeloid-derived suppressor cells and other immunosuppressive cells, severely impairing the therapeutic efficacy of immunotherapy via the secretion of anti-inflammatory cytokines, the expression of immune checkpoint molecules, and the direct or indirect inhibition of T lymphocytes (T cells) or natural killer cell

activity [13]. Therefore, developing effective nano-stimulators with the capacity to promote ICD and modulate TIME for NIR-II photoimmunotherapy against solid tumors is still highly desirable.

The oncology study revealed that TIME is related to the dynamic heterogeneous structures and pathological microenvironment of solid tumors [14, 15]. Typically, the rapid proliferation of tumor cells accompanied by poor vascularization creates hypoxic and necrotic areas more than 100 μm from blood vessels [16]. In this hypoxic environment, hypoxia-inducible factor-1 α (HIF-1 α) can promote programmed cell death ligand-1 (PD-L1) expression in cancer cells and facilitate the recruitment of protumor M2 type TAMs to TIME [17]. This is because macrophages are very sensitive to oxygen fluctuations and preferentially develop to be the M1 type under normoxia vs. M2 type under hypoxia [18]. Moreover, hypoxia inhibits the recruitment of T cells to the tumor area and regulates various aspects of T-cell function, such as metabolism [19], which exacerbates the formation of TIME. For example, the hypoxic region of prostate cancer lacks substantial infiltration of any type of T cells. Thus, vascular normalization and hypoxia alleviation in solid tumors represent promising alternative ways to comprehensively reverse TIME. Nitric oxide (NO), an important signaling molecule in cardiovascular systems, has a wide range of biological activities, including blood vessel growth, smooth muscle relaxation, ECM loosening [20], wound healing, DNA damage, and platelet blocking [21]. High concentrations of NO (up to micromolar) can directly kill cancer cells and arouse ICD, which stimulates the infiltration of T cells [22]. As a gas immuno-regulator, NO can indirectly reprogram TIME by normalizing the tumor vascular system, enhancing pericyte coverage of tumor vessels and relieving hypoxia in the deep layers of solid tumors [23]. NO can also ameliorate TIME by activating M1 type macrophages [24]. Recently, it has even been reported that the immune regulatory network of NO could synergize with CTLA-4 to improve the immunotherapy outcomes of patients with melanoma [25]. NO shows good diffusive ability and cell membrane permeability, but its instability, short half-life and vulnerability to various biological substances make it difficult to accurately deliver sufficient amount of NO to reach deep tumor sites. Among various NO donors, the S-nitrosothiols (SNO)-responsive [21, 26] release of NO provides an effective pathway for renovation of the deleterious TIME.

Moreover, cell membrane-based biomimetic nanotechnology represents a fascinating avenue to aid synthesized nanomedicine in bypassing various biological barriers, such as the bloodstream, epithelial cell barriers, and immune system [27, 28]. In particular, natural macrophage membrane (MM)-camouflaged nanoparticles

could not only escape macrophage clearance but also be guided to tumor tissue through the interaction of C-C chemokine ligand 2 (CCL2)/CCR2 [29] and $\alpha 4$ /VCAM-1 interactions [30]. Furthermore, the specific targeting ligands anchored into cell membranes confer tumor cell-targeting capacity and improve unsatisfactory uptake efficiency [31]. As an excellent tumor-homing penetrating peptide, CGNKRTR (tLyp-1) contains the C-terminal rule (CendR) motif (R/K)XX (R/K) (X represents any amino acid) and specifically recognizes its receptor neuropilin-1, which is overexpressed on the surface of several tumors (e.g. breast) [32, 33]. Several reports have shown that tLyp-1-functionalized nanocarriers can overcome the tumor stroma and penetrate into the deep center of tumors via transcellular action, resulting in highly efficient targeted phototherapy [33]. In this context, integration with tLyp-1 and MM might be a cooperative way to facilitate the permeabilization of SNO-containing gold nanoplatfoms into solid tumors to achieve efficient immuno-stimulation.

In this study, a type of biomimetic immuno-modulator was developed to achieve efficient NIR-II photothermal and gaseous immunotherapy against solid tumors. The biocompatible GNR with strong absorption in the NIR-II window was grafted with SNO and then coated with tLyp-1-anchored MM to yield **GNR-SNO@MMT**. **GNR-SNO@MMT** targeted and accumulated deep into tumor center and effectively induced ICD to stimulate anticancer immunity under NIR-II laser irradiation. Moreover, the generated photothermal effect as well as endogenous glutathione (GSH) triggers NO release in situ, which significantly increases tumor blood perfusion and revascularization to ameliorate the hypoxia and TIME comprehensively, as demonstrated by a decrease in HIF- α , TAMs type conversion, PD-L1 reduction and cytotoxic T lymphocytes (CTLs) infiltration. Synergistically, the remarkable therapeutic outcome was achieved in 4T1 mouse mammary tumors and deep-sited models. In summary, our study provides a facile and feasible PTAs-based nanoplatfom supplemented with gas immuno-adjuvants for the optimal treatment of intractable solid tumors.

Experimental section

Materials

Chloroauric acid and tetraethyl orthosilicate were purchased from Shanghai Maclean Biochemical Technology Co. Silver nitrate, hexadecyltrimethylammonium bromide (CTAB), 3-mercaptopropyltrimethoxysilane and tert-butyl nitrite were purchased from Shanghai Aladdin Biochemical Technology Co. DSPE-PEG₂₀₀₀-MAL was purchased from Xi'an Ruixi Biotechnology Co. Tumor-homing penetrating peptide (tLyp-1) was purchased from Shanghai Gill Biochemistry Co.

The mouse leukemic monocyte macrophage cell line RAW264.7 was purchased from Cell Bank of Chinese Academy of Sciences (Shanghai), and other cell lines were obtained from the American Type Culture Collection. Mouse mammary carcinoma cells 4T1 were cultured with 1% penicillin-streptomycin and 10% calf serum in Roswell Park Memorial Institute (RPMI)-1640 medium at 37 °C and 0.5% CO₂. RAW 264.7 cells were cultured in dulbecco's modified eagle medium under the same conditions as 4T1 cells. Cell culture reagents were purchased from Gibco, USA. Cell Counting Kit-8 (CCK-8), Diaminofluorescein-FM diacetate (DAF-FM DA), membrane dyes 3,3'-diiodotetramethyl-5-(6-dimethylaminopropyl)carbocyanine perchlorate (DiO) and NO Assay Kit were purchased from Shanghai Beyotime Biotechnology Co. Enzyme-linked immunosorbent assay (ELISA) assay kits were purchased from Neobioscience Biotechnology Co. Antibodies (CD4, PD-L1, HIF-1 α , ND2, CD86, and CD31) were purchased from Wuhan Abclone Biotechnology Co. The CD206 antibody was purchased from Proteintech Group, Inc.

Preparation and characterization of GNR-SNO@MMT

Synthesis of GNR

CTAB (7.29 g) was added to 100 mL of deionized water and stirred at 30 °C until the solution became clear. 100 mL of chloroauric acid solution (0.86 mM) was added to the CTAB solution, and the solution turned golden yellow. After that, 6 mL of silver nitrate solution (4 mM), 0.24 mL of 37% hydrochloric acid solution, and 1.5 mL of ascorbic acid solution were added. After the solution became clear, 0.15 mL of freshly prepared NaBH₄ solution (10 mM) was quickly added. The mixture was left to stand for 5 h at room temperature. The obtained GNR solution was washed three times by centrifugation at 10,000 rpm for 15 min to remove the residual CTAB, and 20 mL of deionized water was added to obtain the GNR solution, which was stored at 4 °C with concentration of 1.0 mg/mL.

Synthesis of GNR@SiO₂

Firstly, CTAB (0.2 g) was dissolved in 15 mL of deionized water and stirred at 30 °C until the solution became clear. 5 mL GNR solution (1.0 mg/mL) was added, and the mixture was stirred for 30 min at 30 °C. Sodium hydroxide (0.2 mL, 0.1 M) solution was added, and the mixture was stirred well. 60 μ L of ethyl orthosilicate (20%) was added three times at 30 min intervals and stirred overnight at 27 °C. The resulting solution was washed with water by centrifugation (10,000 rpm, 10 min, 3 times) to obtain GNR@SiO₂.

Synthesis of GNR@SiO₂-SH

The obtained GNR@SiO₂ solution (dissolved in 5 mL of methanol) was placed in a sealed reaction flask and

sonicated for 10 min to remove dissolved oxygen. Then, 250 μ L of 3-mercaptopropyltrimethoxysilane was added, and the mixture was stirred for 24 h at room temperature. Afterwards, the mixture was centrifuged (10,000 rpm, 10 min), washed with methanol three times and finally dissolved in 5 mL of methanol.

Synthesis of GNR@SiO₂-SNO

The obtained GNR@SiO₂-SH solution was placed in a brown reaction flask, and 500 μ L of tert-butyl nitrite was added quickly. The mixture was stirred at room temperature for 24 h. Then, it was centrifuged (10,000 rpm, 10 min), washed three times with methanol and deionized water, and finally dissolved in 5.0 mL of deionized water to obtain a GNR@SiO₂-SNO solution.

Extraction of macrophage membranes

The RAW264.7 cells (approximately 2×10^7 cells) were washed with phosphate buffered solution (PBS) and collected in a 15 mL centrifuge tube by centrifugation at 1,500 \times g for 3 min. The cells were subsequently resuspended in 1.0 mL of ice-cold PBS and centrifuged at 600 \times g for 5 min at 4 °C, and this process was repeated once to obtain the desired macrophages. A total of 1.0 mL of Membrane Protein Extraction Reagent A containing the protease inhibitor phenylmethylsulfonyl fluoride was added to the centrifuge tube, which was left to stand on ice for 30 min. The suspension was transferred to a glass homogenizer and pound 60 times on ice to break the cells. The suspension was collected and centrifuged at 4 °C (700 \times g, 10 min) to remove the nucleus and unbroken cells. After further centrifugation at 4 °C (14,000 \times g for 30 min), the precipitate was collected to obtain MM fragments. The concentration was detected via the bicinchoninic acid (BCA) assay.

Synthesis of GNR-SNO@MMT

DSPE-PEG₂₀₀₀-MAL (5 μ mol) was reacted with tLyp-1 (6 μ mol) in 5 mL of PBS under stirring overnight at 25 °C to obtain DSPE-PEG-tLyp-1. Then, DSPE-PEG-tLyp-1 was mixed with MM fragments (200 μ g/mL) at a weight ratio of 1:5 (W:W) and sonicated in a water bath for 10 min. GNR@SiO₂-SNO solution (200 μ g/mL, 1 mL) was added, and the mixture was sonicated in an ice bath for another 10 min. The solutions were extruded 11 times through a 400 nm membrane extruder, then centrifuged at 8000 rpm for 10 min and washed three times with deionized water to remove the uncoated membrane debris. GNR-SNO@MMT was collected, dissolved in deionized water, and quantified via inductively coupled plasma-mass spectrometry (ICP-MS).

Characterization of GNR-SNO@MMT

The morphology and particle size of GNR-SNO@MMT were observed via transmission electron microscopy (TEM) images acquired on a JEOL JEM 2100 F (JEOL, Japan). Zeta potential and dynamic light scattering analyses were performed via Zetasizer Nanoseries (Malvern Instruments, Malvern, UK). The changes in particle size and polydispersity index were measured at 0, 6, 12, 24, 48 and 72 h by dispersing GNR-SNO@MMT in PBS and RPMI-1640 medium containing 10% calf serum. The ultraviolet-visible-near-infrared (UV-Vis-NIR) absorption spectra were obtained with a full-wavelength microplate reader (Thermo, USA). To determine whether tLyp-1 and MM are present on the GNR-SNO@MMT surface simultaneously, tLyp-1 was conjugated with rhodamine B (RB), and MM was labeled with DiO. Fluorescence microscopy was employed to observe the colocalization of MM and tLyp-1. Additionally, sodium dodecyl sulfate-polyacrylamide gel electrophoresis (SDS-PAGE) analysis was utilized to character the membrane proteins of GNR-SNO@MMT.

NIR-II photothermal performance of GNR-SNO@MMT

Firstly, the heating profile of GNR-SNO@MMT (25, 50, and 100 $\mu\text{g/mL}$) was detected during irradiation for 10 min at laser power densities of 0.5, 0.75, and 1.0 W/cm^2 , respectively. Then, GNR-SNO@MMT (100 $\mu\text{g/mL}$) was subjected to five cycles of laser on/off (1064 nm, 1.0 W/cm^2 , 10 min) to evaluate the stability of photothermal conversion. The temperature rise of GNR-SNO@MMT was also detected via an infrared thermal imaging camera (FLIR Corporation, USA).

To further detect the influences of tissue on NIR-II photothermal effect, 500 μL of GNR-SNO@MMT (100 $\mu\text{g/mL}$) was covered with different thickness (0, 2, 5, and 10 mm) of chicken on the surface of each tube. Then, they were respectively irradiated by 808 nm and 1064 nm lasers at the power density of 1.0 W/cm^2 , and the solution temperature was recorded within 10 min.

NO release investigation

To detect the photothermally controlled release of NO, GNR-SNO, and GNR-SNO@MMT (100 $\mu\text{g/mL}$) were placed in a 37 °C water bath at two-hour intervals (1064 nm, 1.0 W/cm^2 , 10 min), and 50 μL samples were taken every 0.5 h to determine the NO concentration via the Griess method. To probe the release of NO in response to GSH, GNR-SNO@MMT (1 mg/mL) was added to different concentrations of GSH (0, 5, and 10 mM) at 37 °C and measured at different time points (0, 2, 4, 6, 8, and 12 h) via the same method as above.

Targeted tumor cell internalization and immune escape ability

4T1 cells or RAW 264.7 cells (4×10^4 per dish) were seeded into the confocal dish and incubated for one day until the cells were attached to the dish. The cells were then treated with GNR-fluorescein isothiocyanate (FITC), GNR-FITC@MM, or GNR-FITC@MMT (equiv. $[\text{Au}] = 50 \mu\text{g/mL}$). After 6 h incubation, the cells were fixed with 4% paraformaldehyde for 15 min. Then, they were rinsed three times with PBS and incubated with 500 μL of 4',6-diamidino-2-phenylindole (DAPI) for 10 min. After being rinsed three times with PBS, the cells were imaged under a confocal laser scanning microscopy (CLSM).

In vitro NIR-II photothermal anticancer activity assay

4T1 cells (1×10^4 per well) were seeded in a 96-well plate and treated with GNR@MM, GNR@MMT, GNR-SNO@MM, or GNR-SNO@MMT (equiv. $[\text{Au}] = 50 \mu\text{g/mL}$) for 6 h. After the medium was removed and the cells were washed with PBS, the cells were irradiated (1064 nm, 1.0 W/cm^2 , 5 min) and then incubated for 24 h. Then, the relative cell viability was determined with the CCK-8 kit.

4T1 cells (1×10^5 per well) were seeded into 6-well plates and treated as described above. Then, the cells of each group were collected in centrifuge tubes, centrifuged and stained with calcein-AM/propidium iodide (PI) solution for 30 min. Finally, the sections were observed under a fluorescence inverted microscope.

Immunogenic cell death assay

4T1 cells (4×10^4 per well) were seeded in confocal culture dishes and incubated for 24 h. Then, they were treated with cell culture medium containing GNR@MM, GNR@MMT, GNR-SNO@MM, or GNR-SNO@MMT (equiv. $[\text{Au}] = 50 \mu\text{g/mL}$). After incubation for 12 h, the irradiation groups were treated with a laser (1064 nm, 1.0 W/cm^2 , 5 min). After another incubation for 4 h, the culture medium was aspirated, and the cells were fixed with paraformaldehyde for 30 min. After removing paraformaldehyde, the cells were blocked with 1% BSA at 37 °C for 30 min. Following washing with PBS, the cells were further incubated overnight at 4°C with a calreticulin (CRT) antibody. Then, the cells were washed with PBS before being incubated with an Alexa 488-conjugated secondary antibody for 2 h in the dark. The secondary antibody was then aspirated, and the cells were washed with PBS, followed by incubation with DAPI staining solution for 20 min in the dark. Then the DAPI solution was aspirated. Finally, the cells were washed with PBS and observed via CLSM.

To detect high-mobility group box 1 (HMGB-1) release, 4T1 cells were treated as described above and incubated for 24 h, and afterwards the culture medium was

collected. The HMGB-1 content in the culture medium was measured according to the instructions of ELISA kit.

Intracellular NO measurement

4T1 cells (1×10^5 per well) seeded in a 6-well plate were treated with GNR@MM, GNR@MMT, GNR-SNO@MM, or GNR-SNO@MMT (equiv. [Au] = 50 $\mu\text{g}/\text{mL}$) for 6 h. After discarding cell culture medium, the cells were washed with PBS three times and then incubated with the DAF-FM DA probe for 20 min. The irradiated groups were exposed to laser irradiation (1064 nm, 1.0 W/cm^2 , 5 min). Afterwards, the cells were fixed with paraformaldehyde for 30 min and then observed under a fluorescence microscope.

WB assay of PD-L1 expression

4T1 cells (1×10^5 per well) seeded in a 6-well plate were incubated in a hypoxic incubator for 48 h, whereas those in the control group were incubated in a normoxic incubator. The cells were subsequently treated with GNR@MMT or GNR-SNO@MMT (equiv. [Au] = 50 $\mu\text{g}/\text{mL}$) for 6 h and then irradiated with a laser (1064 nm, 1.0 W/cm^2 , 5 min). The control group was incubated with PBS for 6 h. After another incubation for 24 h, the cells were lysed with ice-cold lysis buffer and sonicated. The lysates were centrifuged, and the supernatant was collected as the total protein extract. The protein concentration was determined via the BCA method. Protein samples were mixed with 5 \times loading buffer at a 1:4 ratio and stored at -20°C .

For SDS-PAGE, a 7.5% separating gel and a 5% stacking gel were prepared. Protein samples (25 μg) and marker were loaded into the wells. Electrophoresis was performed at 80 V for the stacking gel and 120 V for the separating gel.

The proteins were subsequently transferred from the gel to a polyvinylidene fluoride (PVDF) membrane. The PVDF membrane was blocked with blocking solution, incubated with PD-L1 antibody overnight at 4°C , and then incubated with secondary antibody for 2 h at room temperature. Detection was performed via the use of an enhanced chemiluminescence substrate, and the proteins were quantified via Image J.

In vivo fluorescence imaging and biodistribution studies

4T1 cells (1.0×10^6 per mouse) were injected subcutaneously into the right leg of BALB/c female mice, and when the tumor volume reached approximately 100 mm^3 (recorded as Day 0), 100 μL of free indocyanine green (ICG), GNR-ICG@MM or GNR-ICG@MMT (at the equiv. [ICG] = 20 $\mu\text{g}/\text{mouse}$) was injected via tail vein. The fluorescence was imaged in an in vivo small animal fluorescence imaging system (Lumina Series III imaging, USA) at 0 h, 2 h, 4 h, 8 h, 24 h, and 48 h

post-administration. After 48 h, the mice were sacrificed, and the heart, liver, spleen, lungs, kidneys and tumors were isolated for imaging.

In vivo NIR-II photothermal-NO combination antitumor study

The 4T1 tumor mouse model was constructed and divided into seven groups: (G1) saline, (G2) saline + L, (G3) GNR-SNO@MMT, (G4) GNR@MMT + L, (G5) GNR-SNO@MM + L, (G6) GNR-SNO@MMT + L, and (G7) GNR-SNO@MMT + L + 5 mm chicken. Each formulation (100 μL) was administered via tail vein (equiv. [Au] = 100 $\mu\text{g}/\text{each}$, [NO] = 23.6 nmol/each) on days 0, 3, and 6. Laser irradiation (1064 nm, 1.0 W/cm^2 , 5 min) was performed on days 1, 4, and 7, respectively. The tumor volume (tumor volume = length \times width² \times 0.5) and mouse body weight were recorded every 2 days during the treatment period. On day 10, the level of cytokines like interleukin-10 (IL-10), interleukin-6 (IL-6), interferon gamma (IFN- γ) and tumor necrosis factor- α (TNF- α) in serum were measured with an ELISA kit. On day 15, the mice were sacrificed, and the blood was analyzed for routine test, liver and kidney function. The heart, liver, spleen, lung, and kidney were dissected for Hematoxylin and Eosin (H&E) staining to study the biosafety of the nanosystem. The isolated tumors were photographed and weighed, and the tumor sections were subjected to H&E, and terminal-deoxynucleotidyl transferase mediated nick end labeling (TUNEL) staining.

In vivo immune cascade and suppressive TIME detection

Dendritic cells (DCs) maturation assay On day 10, the mice were sacrificed, and the drained lymph nodes were dissociated under aseptic conditions and placed in a sterile dish containing culture medium. The lymph nodes were chopped with sterile surgical scissors and then ground with the inner core of a syringe until white flocculent. The resulting mixture was filtered through a 74 μm sterile nylon mesh. The cell suspension was centrifuged at 4°C , and the cell precipitate was collected and resuspended in prechilled PBS in an ice bath. Then, the samples were transferred to a 1.5 mL centrifuge tube, centrifuged, washed, and stained with anti-CD11C, anti-CD80, and anti-CD86 antibodies for flow cytometry analysis.

Spleen T-cell assay On day 15, the mice were sacrificed, and the spleens were dissociated under aseptic conditions and placed in sterile dishes with culture medium. The resulting mixture was filtered through a 74 μm sterile nylon mesh, and the red blood cells were broken up with erythrocyte lysis solution. After termination, the cell suspension was centrifuged at 4°C , and the cell precipitate was collected. After being resuspended in precooled PBS in an ice bath, the cells were transferred to a 1.5 mL cen-

trifuge tube, centrifuged, washed and stained with CD3, CD4 and CD8 antibodies for flow cytometry analysis.

TIME analysis

On day 10, after the mice were sacrificed, the dissociated tumors were kept in paraformaldehyde under aseptic conditions. Immunohistochemical analysis was performed on tumor sections to detect the expression of HIF-1 α and PD-L1. Tumor-associated macrophages (CD206:M2 type, CD86:M1 type), blood vesicles (CD31) and pericytes (NG2) were analyzed by immunofluorescence.

In vivo vascular permeability study

A 4T1 subcutaneous tumor model was established, and when the tumor volume reached 800–1000 mm³, the mice were injected with Evans blue staining solution through the tail vein. After 2 h, the mice were divided into four groups: (G1) saline, (G2) **GNR-SNO@MMT**, (G3) **GNR@MMT**+L and (G4) **GNR-SNO@MMT**+L (equiv. [Au] = 100 μ g/mouse, [NO] = 23.6 nmol/mouse). Laser irradiation (1064 nm, 1.0 W/cm², 5 min) was performed at 24 h post-administration. After another 10 h, the mice were dissected, and the tumor tissues were removed and immersed in N, N-dimethylformamide. The absorbance of Evans blue at 620 nm was measured after 24 h for quantitative analysis.

Statistical analysis

All the results are expressed as the means \pm standard deviations (SDs). ANOVA was performed via GraphPad Prism software to statistically analyze the experimental data between different groups. Statistical significance is indicated as * ($p < 0.05$), ** ($p < 0.01$), *** ($p < 0.001$), and **** ($p < 0.0001$).

Results and discussion

Construction and characterization of GNR-SNO@MMT

The procedures to prepare the biomimetic nano-modulator **GNR-SNO@MMT** are shown in graphical abstract. GNR with larger aspect ratios were synthesized via a one-pot method with some modification [34]. As shown in Fig. 1A, the TEM images showed that the synthesized GNR were 54 ± 4 nm and 8 ± 3 nm in length and width respectively, with a high aspect ratio of 7:1. Subsequently, a mesoporous silica layer (8 ± 1 nm thick) was grown on GNR. Then, they were modified with -SH and reacted with tert-butyl nitrite to attach -SNO side chains (Fig. 1B). High-angle annular dark field scanning transmission electron microscopy and energy dispersive spectrometry elemental analysis revealed that GNR-SiO₂-SNO (referred as GNR-SNO) contained Au, S, Si, O, and N (Fig. 1C and Figure S1A). And Au element was located in the inner part, while Si element was wrapped in the outer part. The specific N element representing the -SNO

side chain appeared on the surface, which confirmed the successful synthesis of GNR-SNO. The UV-Vis-NIR spectra revealed that both GNR and GNR-SNO with obvious NIR-II LSPR absorption peaks at approximately 930 nm (Fig. 1D). ICP-MS analysis revealed that the content of Au in GNR-SNO was 33.0%. To confer the stability, tumor-targeting ability and macrophage escape ability of GNR-SNO, MM was coated around GNR-SNO (at a mass ratio of GNR/MM = 1/1). The TEM images revealed a thin cell membrane visible on the surface of GNR-SNO@MM (Fig. 1E). It featured protein bands similar to those of MM fragments as shown in SDS-PAGE (Fig. 1F), suggesting that many membrane proteins are preserved in GNR-SNO@MM. The redshift in the absorption spectrum of GNR-SNO@MM (980 nm) further demonstrated the success of membrane coating (Fig. 1D). In addition, the changes in the hydrodynamic diameter and zeta potential of GNR, GNR-SNO, and GNR-SNO@MM demonstrated the sequential modifications (Fig. 1G and Figure S1B). GNR-SNO@MM owned the negative charge (ca. -35.8 mV) (Fig. S1B). Finally, the peptide tLyp-1 was mosaicked on GNR-SNO@MM to confer the tumor-targeting and deep penetration ability. The green fluorescence of DiO (labeling MM) and red fluorescence from tLyp-1-RB strongly overlapped, suggesting successful anchoring of tLyp-1 (c.a. 0.1 μ g/ μ g) on **GNR-SNO@MMT** (Fig. 1H). In addition, the fluorescence spectrum at 605 nm of **GNR-SNO@MMT** further verified successful conjugation (Figure S1C). The modification did not affect the size or zeta potential of **GNR-SNO@MMT** (Fig. 1G and Figure S1B). **GNR-SNO@MMT** showed excellent stability in both PBS and cell culture medium containing 10% calf serum for 96 h (Figure S1D), which guaranteed its in vivo NIR-II photothermal therapy (PTT) application.

Next, we characterized the NIR-II photothermal conversion performance of **GNR-SNO@MMT**, which was dose- and laser power density-dependent (Figure S1E-F). When the concentration reached 100 μ g/mL, the solution temperature increased sharply to 35.7 $^{\circ}$ C within 5 min, and the maximum temperature reached 61.9 $^{\circ}$ C under irradiation (1064 nm, 1.0 W/cm², 10 min) (Fig. 2A). Moreover, the temperature-time curve and peak shape of **GNR-SNO@MMT** (Fig. 2B) did not obviously change after five cycles of laser irradiation and cooling, suggesting the extraordinary photothermal conversion stability of **GNR-SNO@MMT**. Specifically, we compared the photothermal conversion performance of **GNR-SNO@MMT** with that of irradiation by an NIR-II laser (1064 nm, 1.0 W/cm², 10 min) and NIR-I (808 nm, 1.0 W/cm², 10 min) at the same concentration (100 μ g/mL) under the shielding of different thicknesses of chicken, which were placed between the laser and **GNR-SNO@MMT** solutions, to simulate the depth of tissue penetration. As shown in Fig. 2C, the NIR-II laser (1064 nm)

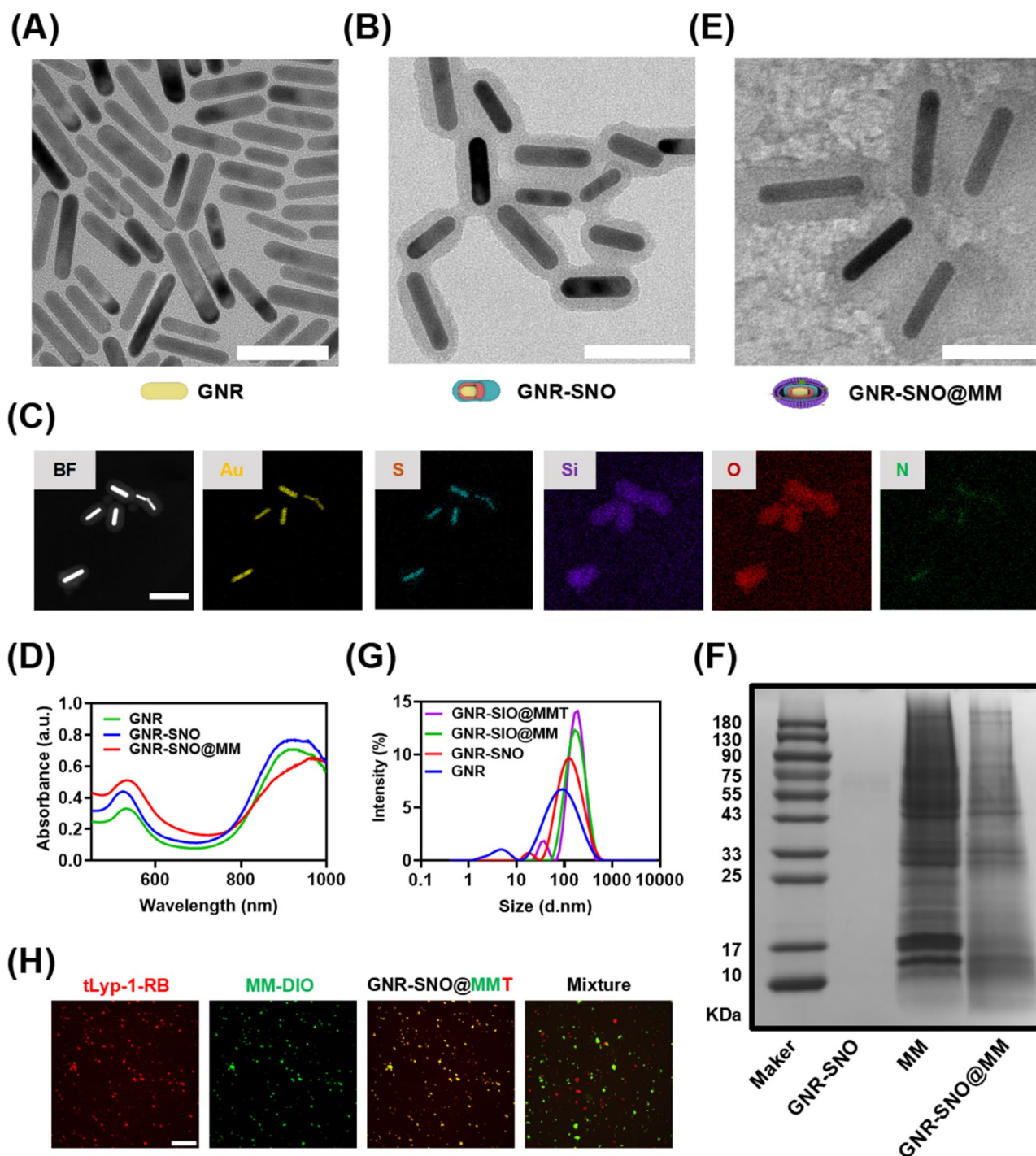


Fig. 1 Construction and characterization of **GNR-SNO@MMT**. TEM images of (A) GNR and (B) GNR-SNO (scale bar: 50 nm). (C) Elemental mapping of GNR-SNO (scale bar: 100 nm). (D) UV- vis-NIR absorption spectra and (E) TEM image of GNR-SNO@MM (scale bar: 50 nm). (F) SDS-PAGE analysis of GNR-SNO, MM, and GNR-SNO@MM. (G) Hydrodynamic diameter and (H) fluorescence colocalization results of **GNR-SNO@MMT** (scale bar: 200 μ m)

induced a much greater increase in temperature than did the NIR-I laser (808 nm) at each thickness of chicken. For example, the temperature was increased by 6.6 $^{\circ}$ C under the shielding of chicken (thickness of 10 mm), whereas the temperature was not substantially increased under irradiation by an 808 nm laser (1 W/cm², 10 min) under

the same conditions. Therefore, the results showed that GNR-SNO@MMT could be very beneficial for NIR-II PTT treatment of both superficial and deep tumors.

The hyperthermia effect promoted the homolytic cleavage of the S-N bond in SNO, accelerating NO release. Figure 2D showed that the NIR-II photothermal effect of

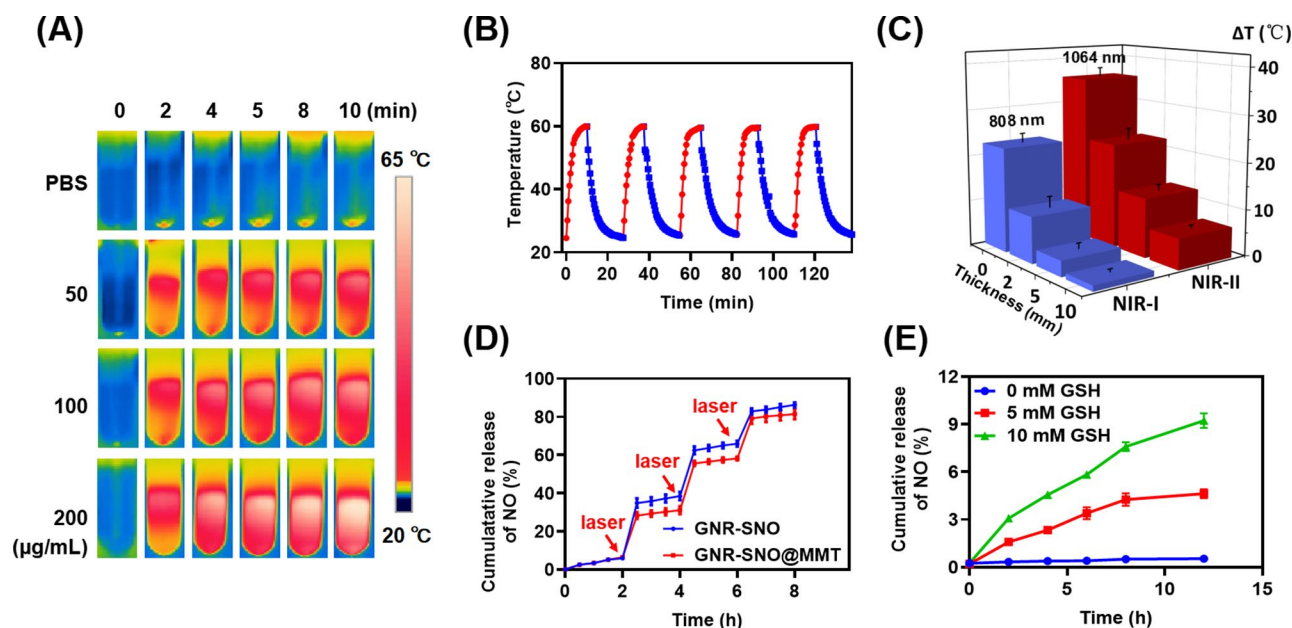


Fig. 2 (A) IR thermal images of **GNR-SNO@MMT** aqueous solutions with different concentrations under NIR-II irradiation (1064 nm, 1.0 W/cm², 10 min). (B) Photothermal stability of **GNR-SNO@MMT**. (C) Photothermal effects of **GNR-SNO@MMT** (100 µg/mL) under different thickness of chicken and NIR-I (808 nm) /NIR-II (1064 nm) irradiation (1.0 W/cm², 10 min). (D) Cumulative release rates of NO from GNR-SNO and **GNR-SNO@MMT** after irradiation with an NIR-II laser (1064 nm, 1.0 W/cm², 10 min). (E) Cumulative release rate of NO from **GNR-SNO@MMT** in the presence of GSH

GNR-SNO@MMT could accelerated NO release. And 89% NO was finally released after three cycles of NIR-II laser irradiation (1064 nm, 1.0 W/cm², 10 min). It was calculated that 1 mg of **GNR-SNO@MMT** could release about 70.7 nmol of NO, similar to the unmodified GNR-SNO. In addition, NO can be released in the presence of GSH [21] whose concentration in tumor cells (2~10 mM) is approximately 1,000-fold greater than that of the extracellular environment (2~20 µM) [35]. As shown in Fig. 2E, there was hardly any NO release in the absence of GSH, whereas accelerated NO release with increasing GSH concentration was observed. **GNR-SNO@MMT** released approximately 9.2% of NO in the presence of 10 mM GSH. These results suggested that the biomimetic membrane had no significant effect on the NO release capacity. Overall, the nanosystem **GNR-SNO@MMT** could be a controlled NO reservoir for the combination of NIR-II PTT and NO modulation.

In vitro-targeted NIR-II PTT efficiency of **GNR-SNO@MMT**

To verify the targeted endocytosis, we co-cultured 4T1 tumor cells with FITC labelled formulation for 6 h and found that the intracellular green fluorescence in GNR-FITC@MM treated group was much greater than that in GNR-FITC treated group (Fig. 3A-B). In particular, the intracellular fluorescence intensity for GNR-FITC@MMT treated group was highest in the three groups, suggesting that tLyP-1 could further facilitate the cellular uptake. However, GNR-FITC@MM and GNR-FITC@MMT could hardly be phagocytosed by macrophages

since very dim intracellular fluorescence signals were observed for GNR-FITC@MM and GNR-FITC@MMT treated RAW 264.7 cells. However, GNR-FITC was obviously endocytosed by RAW264.7 cells. These observations verified the tumor targeting and immune escaping behavior of **GNR-SNO@MMT** camouflaged by MM. Moreover, the deep penetration effect of **GNR-SNO@MMT** in a tumor sphere model was analyzed via CLSM in 2.5D layer scan mode. As shown in Fig. 3C, GNR-FITC@MMT was able to penetrate into the deeper position of the tumor sphere at approximately 70 µm. GNR-FITC@MM and GNR-FITC were distributed only at the surface layer of the tumor spheroids since only a slight fluorescent signal was observed there. Therefore, the tumor-homing peptide tLyP-1 confers a pronounced tumor-targeting penetration ability to **GNR-SNO@MMT**, which would favor the NIR-II PTT application.

Moreover, intracellular NO production was investigated with a DAF-FM DA probe (Fig. 3D). And no obvious green fluorescence was observed in the PBS or GNR@MMT treated groups in the absence of irradiation. In GNR-SNO@MM treated group, little green fluorescence was observed in the cytoplasm, suggesting that a limited amount of NO was released from SNO in response to intracellular GSH [21]. However, a significant increase of the green fluorescence signal was observed in **GNR-SNO@MMT** treated group, which may be related to enhanced endocytosis with aid of tLyP-1. Particularly, after irradiation, the GNR-SNO@MM treated group presented markedly increased intracellular green

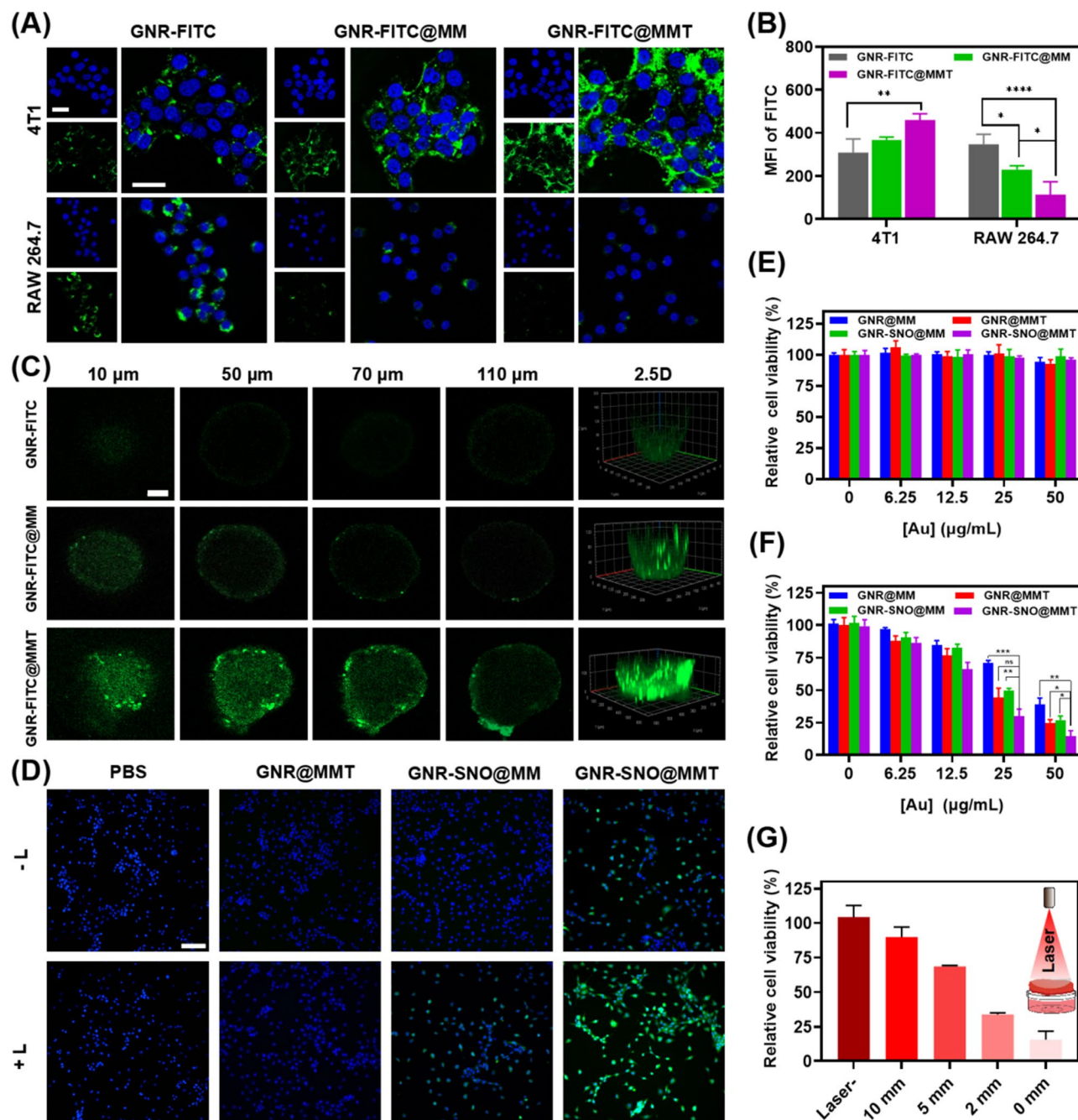


Fig. 3 **(A)** Representative CLSM images of the cellular uptake of GNR-SNO@MMT by 4T1 tumor cells and RAW264.7 cells after 6 h of incubation (scale bar: 20 μm) and **(B)** further quantification via Image J. **(C)** CLSM images and 2.5D reconstructed images of GNR-FITC, GNR-FITC@MM, and GNR-FITC@MMT treated 4T1 tumor spheres after 6 h (scale bar: 50 μm). **(D)** Fluorescence microscopy observation of NO release in 4T1 tumor cells after different treatments (nucleus: blue fluorescence, DAF-FM DA: green fluorescence, scale bar: 100 μm). Relative cell viability of 4T1 cells treated with **GNR-SNO@MMT** and the relevant controls **(E)** in the dark and **(F)** under laser irradiation. **(G)** Relative cell viability of 4T1 cells after endocytosis of **GNR-SNO@MMT** under different thickness of chicken and laser irradiation (1064 nm, 1.0 W/cm², 5 min)

fluorescence. As expected, the highest level of intracellular green fluorescence was observed in **GNR-SNO@MMT+L** treated group, demonstrating that the PTT effect and tLyP-1 could indeed favor endocytosis and help release intracellular NO.

The anticancer activity of **GNR-SNO@MMT** at the cellular level was then investigated. Without irradiation, it induced negligible cytotoxicity to 4T1 cells (Fig. 3E) and other cell lines (i.e., MCF-10 A and RAW 264.7) (Figure S2A-B). Upon NIR-II laser irradiation, **GNR-SNO@MMT** caused significant cell death (Fig. 3F) in

a dose-dependent manner. When the equivalent [Au] reached 50 $\mu\text{g}/\text{mL}$, the cell viability of the **GNR-SNO@MMT**+L group decreased sharply to 14.5%, whereas the survival rates of the nontargeted groups (GNR-SNO@MM+L) and the NO-free group (GNR@MMT+L) were 24.9% and 26.9% respectively. Also, we observed a similar photothermal antitumor capacity in the human breast cancer cell line MDA-MB-231 (Figure S2C-D). Additionally, typical calcein-AM/PI staining results confirmed that **GNR-SNO@MMT**+L induced tumor cell death (Figure S2E). Therefore, **GNR-SNO@MMT** exhibited targeted and combined tumoricidal effects via NIR-II PTT and NO gas therapy. Furthermore, to verify whether the NIR-II laser could penetrate deep into tissues to achieve deep tumor killing effects, chicken of different thickness were used to simulate the tumor depth, and the cell viability was examined after laser irradiation (Fig. 3G). **GNR-SNO@MMT** still had an excellent killing effect on 4T1 cells under the shielding of chicken. Therefore, **GNR-SNO@MMT** has excellent NIR-II-targeted photothermal antitumor effects.

Activated photo-immunity and NO-regulated immunosuppression by **GNR-SNO@MMT**

To further detect the immuno-stimulatory effect of **GNR-SNO@MMT**, we measured ICD markers by immunofluorescence and ELISA. CRT on the surface of dying tumor cells generate an “eat me” signal for antigen-presenting cells DCs to activate the immune system. HMGB-1 is released from dying tumor cells to stimulate DCs [36]. As shown in Fig. 4A-B, compared with the unirradiated groups, GNR@MM+L treated group presented obvious immunofluorescence of CRT resulting from the NIR-II PTT effect. NO release slightly affected the ICD effect since similar immunofluorescence of CRT was observed GNR-SNO@MM+L treated group. However, in GNR@MMT+L treated group, stronger immunofluorescence intensity was observed, which was mostly attributed to the targeted NIR-II PTT aided by tLyP-1. Expectedly, **GNR-SNO@MMT**+L treatment induced the most CRT exposure. Moreover, the release of HMGB-1 from tumor cells upon different treatment showed a trend similar to that of CRT (Fig. 4C). Clearly, **GNR-SNO@MMT** effectively evoked prominent anticancer immune activity.

Moreover, we detected the effects of **GNR-SNO@MMT** on the expression of PD-L1 under hypoxia in the absence and presence of irradiation. A significant increase in PD-L1 expression was observed in tumor cells under hypoxia (Fig. 4D-E), which was in accordance with the previous report [14]. Additional photothermal stimulation mediated by GNR@MMT+L treatment further led to an increase of PD-L1 expression because of the high level of IFN- γ during PTT [37]. However, the expression of PD-L1 was obviously reduced in **GNR-SNO@**

MMT+L treated group. And the underlying rationale was that NO gas, an important signaling molecule, inhibited the activation of HIF-1 α and thus resisted the expression of PD-L1 [38] mostly probably through the direct and indirect mechanisms (STAT3/VEGF pathway) [14]. Additionally, NO has been reported to suppress the activity of Sp1 transcription factor, which binds to the PD-L1 promoter and mediates PD-L1 expression [16, 39]. Thus, these data suggested that **GNR-SNO@MMT** was an effective immunomodulator via NO gaseous blocking of the PD-L1/PD-1 axis.

Assessment of the distribution and vascular permeability of **GNR-SNO@MMT**

To visualize the biodistribution of **GNR-SNO@MMT** in tumor-bearing mice, ICG-labeled formulation was i.v. injected into 4T1 subcutaneous mice models. The fluorescence signals emerged in each group 2 h after administration (Fig. 5A). More pronounced fluorescence accumulation was observed in GNR-ICG@MM and GNR-ICG@MMT treated groups after 4 h than in the free ICG group, presumably due to the nanoformulation mediated enhanced permeability and retention (EPR) effect and tumor-inflammatory tropism of the MM modification [40]. The high fluorescence signals at the tumor site in the GNR-ICG@MM group and the GNR-ICG@MMT group were maintained until 8 h post-injection and then gradually weakened (Fig. 5B). Ex vivo biofluorescence imaging and quantification of the main organs after 48 h revealed that the GNR-ICG@MM and GNR-ICG@MMT groups still presented fluorescence signals at the tumor site at 48 h (Fig. 5C). To note, the fluorescence signal in tumor of GNR-ICG@MMT treated group was greatly enhanced (2.7-fold of free ICG group). There was almost no significant biofluorescence signal in other organs except the liver. Taken together, the modification of MM and tLyP-1 peptide endowed GNR-ICG@MMT the ability of tumor targeting and penetrating. Moreover, infrared thermography was used to monitor the in vivo NIR-II photothermal conversion of **GNR-SNO@MMT** after accumulation at tumor sites. As shown in Fig. 5D, **GNR-SNO@MMT** increased the temperature to 55 $^{\circ}\text{C}$ within 5 min, which was much higher than the 42 $^{\circ}\text{C}$ temperature for the GNR-SNO@MM group, whereas no significant temperature change occurred at the tumor site for the saline group (Fig. 5E). These results confirmed that **GNR-SNO@MMT** could serve as an optimal NIR-II photothermal agent for tumor ablation.

NO plays an important role in vascular smooth muscle. It enhances vascular permeability and blood flow to increase the accumulation of nanoparticles in tumor [41]. Intravenous injection of Evans blue dye could bind to albumin and penetrate tumors in vivo and widely be used to evaluate whether enhanced EPR effect occurred

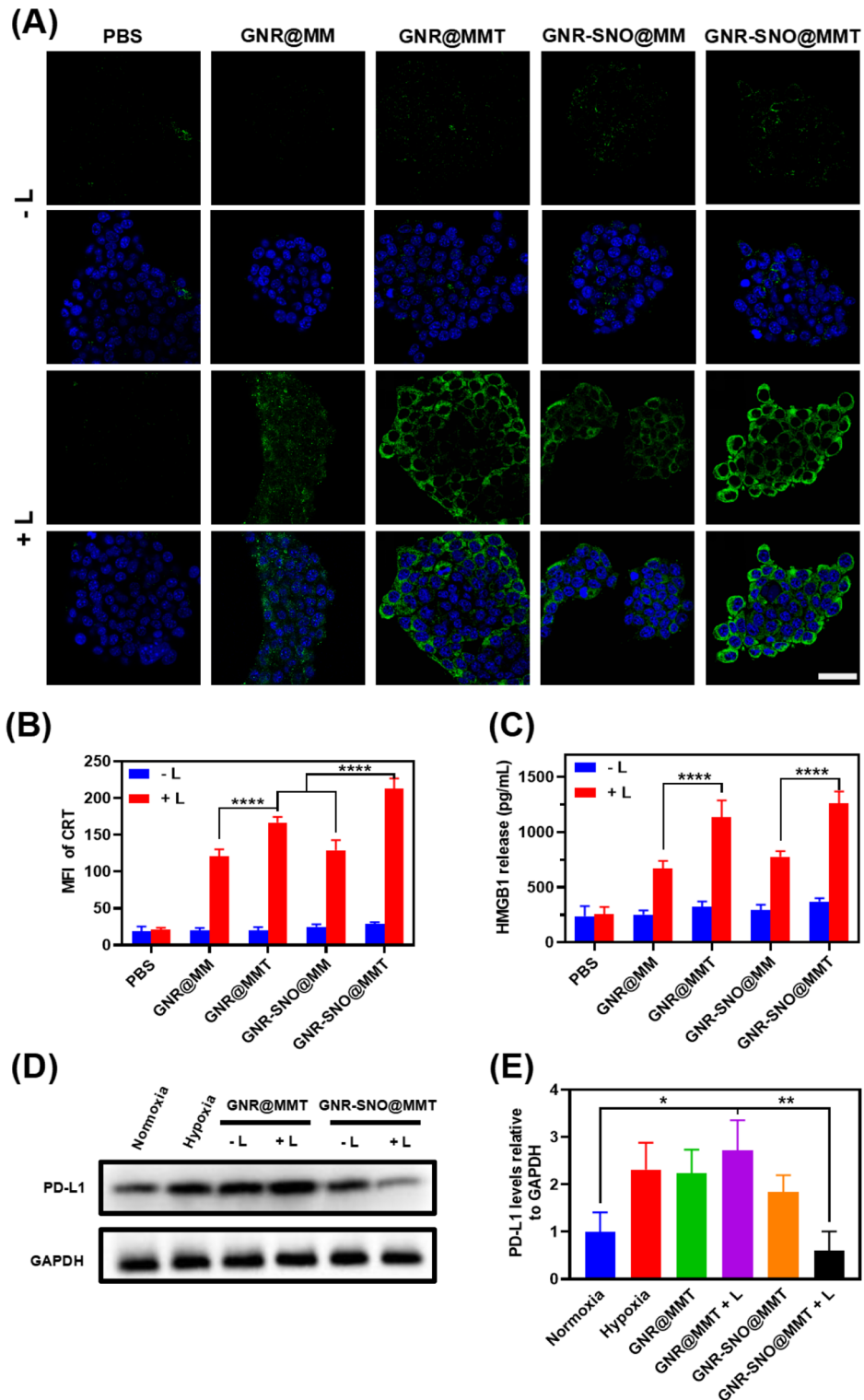


Fig. 4 (A) CLSM observation of CRT exposure in 4T1 cells after different treatments (nucleus: blue fluorescence; CRT: green fluorescence; scale bar: 40 μm). (B) Quantitative comparison of the fluorescence intensity of CRT. (C) ELISA detection of HMGB-1 releases from tumor cells after different treatments (1064 nm, 1.0 W/cm², 5 min). (D) WB assay and (E) quantitative analysis of PD-L1 expression in 4T1 cells after different treatment

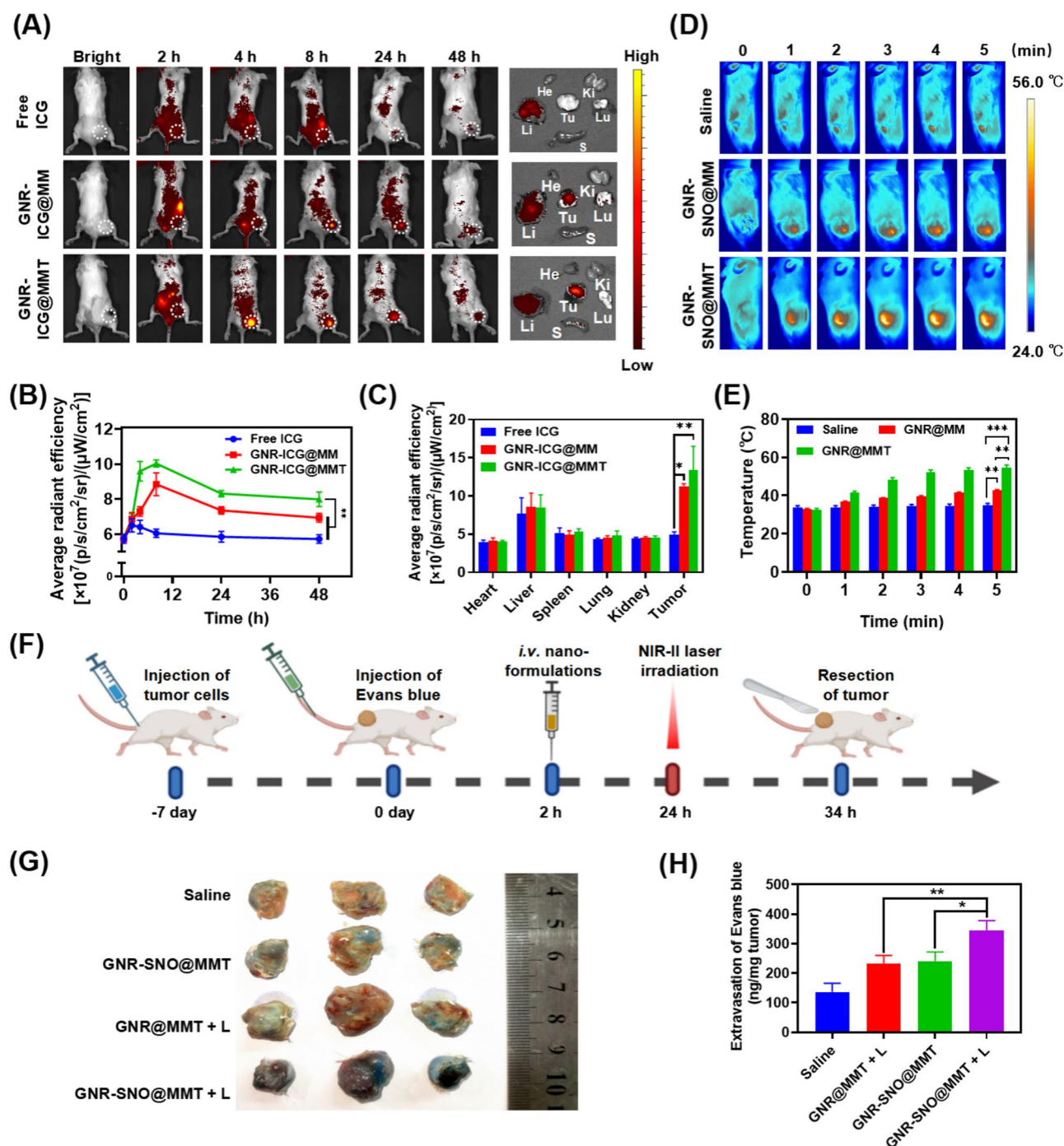


Fig. 5 In vivo tumor accumulation capacity and vascular permeability assay. **(A)** in vivo fluorescence images of tumor-bearing mice after treatment with **GNR-SNO@MMT** for different durations and ex-vivo fluorescence images of various organs and tumors. **(B)** Time course of tumor fluorescence intensity of tumor-bearing mice treated with **GNR-SNO@MMT**. **(C)** The fluorescence intensity of main organs and tumor after 48 h. **(D)** Whole-body IR thermograms of **GNR-SNO@MMT** and control-treated tumor-bearing mice (1064 nm, 1.0 W/cm², 5 min). **(E)** Temperature at tumor site of tumor-bearing mice after laser exposure. **(F)** Flow chart of tumor vascular permeability assay. **(G)** Evans blue dye in the tumor tissue and **(H)** quantification after tumor-bearing mice were treated with different nanoformulations

after **GNR-SNO@MMT** treatment (Fig. 5F). As shown in Fig. 5G, only a limited amount of Evans blue dye penetrated the tumor vessels and reached the tumor in saline group. Satisfactorily, more Evans blue dye penetrated the

tumor in **GNR@MMT + L** treated group, attributing to the photothermal effect. In addition, **GNR-SNO@MMT** without laser irradiation also enhanced Evans blue dye extravasation due to NO release response to endogenous

GSH. As expected, the **GNR-SNO@MMT+L** group, owing to the combined effect of NIR-II PTT with NO, presented much greater Evans blue dye extravasation than other two treated groups (Fig. 5H). Thus, **GNR-SNO@MMT** could be used as a vasodilator in the tumor vasculature as well as an enhancer of EPR effect, which would further promote the accumulation of the therapeutic agent in the tumor site.

In vivo NIR-II/gas combined anti-tumor efficiency of GNR-SNO@MMT

To dissect the synergistic photo-immunotherapy of **GNR-SNO@MMT** in vivo, we established a 4T1 subcutaneous tumor model in the right hind limb of BALB/c mice. This model was meticulously divided into seven distinct cohorts: (G1) saline, (G2) saline + L, (G3) **GNR-SNO@MMT**, (G4) **GNR@MMT** + L, (G5) **GNR-SNO@MM** + L, (G6) **GNR-SNO@MMT** + L, and (G7) **GNR-SNO@MMT** + L with a layer of chicken (5 mm) to mimic deep tissue (Fig. 6A). A consistent tumor growth

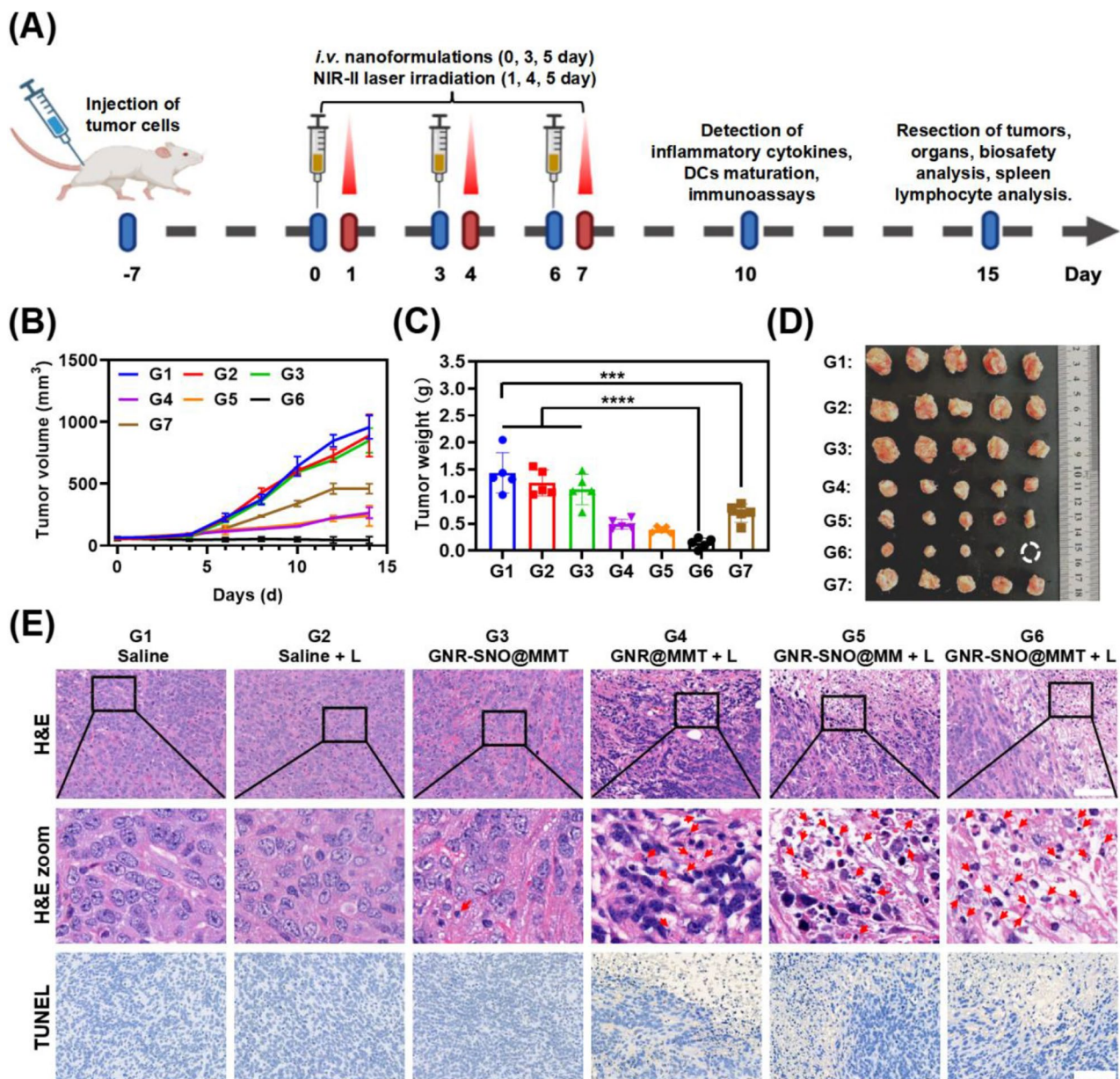


Fig. 6 NIR-II photothermal-NO-immune antitumor effects. **(A)** Flow chart of in vivo treatment. **(B)** Tumor volume growth curves of treated groups. **(C)** Tumor weights and **(D)** digital photographs of the tumors. **(E)** H&E, H&E zoom (red arrows represent tumor cells with nuclear crumpling, apoptosis or necrosis), and TUNEL staining (scale bar: 100 μm) of tumor tissues

pattern were monitored over a span of 15 days for both the control (G1) and laser alone treated (G2) group, and NO monotreatment (G3: **GNR-SNO@MMT** alone) was insufficient to suppress tumor progression (Fig. 6B-C). Notably, the treatment with **GNR@MMT+L** (G4) exhibited marked inhibition of tumor growth (c.a. 68.8%), which was predominantly attributed to the PTT effect. Similarly, the non-targeted treatment with **GNR-SNO@MM+L** (G5) demonstrated comparable inhibition effect (c.a.75.2%). Strikingly, the group receiving **GNR-SNO@MMT+L** (G6) presented the most remarkable tumor growth inhibition, with an inhibition rate of 94.7%, which surpassed all the other groups (Figure S3A). This data underscores the potentiated antitumor efficacy conferred by the synergistic NIR-II photothermal effect and stimulated NO release. Notably, the group treated with **GNR-SNO@MMT+L** and chicken (G7) exhibited significant regression of tumor growth, confirming the capacity of the NIR-II laser (1064 nm) to effectively inhibit deeply seated tumors.

No obvious weight fluctuations were observed in any of the mice during the treatment period (Figure S3B). Furthermore, at the end of treatment, the mice were sacrificed, and the tumors were photographed and weighed. As shown in Fig. 6D, the changes in tumor size were consistent with the changes in tumor volume. The tumor sections were subsequently stained with H&E, and TUNEL to assess tumor proliferation and apoptosis/necrosis after different treatments (Fig. 6E). In the H&E zoom image, the apoptotic or necrotic tumor cells that underwent nuclear crumpling by red arrows was marked. Large areas of tumor cells were broken and cytolysis occurred, and fewer proliferated cells were observed in the **GNR-SNO@MMT+L** (G6) group than in **GNR@MMT+L**(G4) and **GNR-SNO@MM+L** (G5) treated groups. However, in the other two groups, **GNR@MMT+L** (G3) and saline+L (G2), little or no damage to the tumor cells occurred. These data indicated that the **GNR-SNO@MMT**-mediated NIR-II PTT and NO release had excellent anticancer effects. Taken together, these findings indicate that the NIR-II-responsive and targeted **GNR-SNO@MMT** is promising for controlled and combined cancer treatment.

Antitumor immune cascade and reshaping of the microenvironment

To explore the mechanism by which **GNR-SNO@MMT** strongly inhibited tumor growth, the maturation of DCs in the draining lymph nodes of the mice was examined. Compared with the saline (G1) and the laser group (G2) (Fig. 7A-B), and **GNR-SNO@MMT** alone (G3) groups hardly induced DCs maturation, but the single-targeted NIR-II PTT group (**GNR@MMT+L**, G4) caused 22.4% ± 2.7% DCs maturation, which was due to the ICD effect.

However, the NIR-II PTT-NO treatment (**GNR-SNO@MMT+L**, G6) significantly promoted the maturation of DCs, with the proportion of CD80⁺ CD86⁺ DCs reaching 34.7% ± 3.9%. This ratio was also much greater than that of the nontargeted PTT-Gas treatment (**GNR-SNO@MM+L**, G5), only with 16.0% ± 0.7% DCs maturation. The integration of MM and tLyP-1 into our nanoplat-form significantly enhanced the combined PTT and NO release effect. Indeed, NIR-II PTT not only triggers ICD but also substantially stimulates the release of NO. This concerted action helped mitigate tumor hypoxia, thereby potentiating the photo-immune antitumor response. Moreover, we detected the activation of T cells in the spleens of the mice and found that the frequencies of CD8⁺ T cells (Fig. 7C-D) and CD4⁺ T cells (Fig. 7E-F) were significantly greater in the PTT (G4) and PTT-Gas combined-treated groups (G5-G6). The targeted PTT-NO combined treatment mediated by the **GNR-SNO@MMT+L** group had the highest ratio of CD8⁺ T cells (18.7% ± 5.4%) and CD4⁺ T cells (25.3% ± 5.9%), which was mostly related to DCs maturation. These findings further demonstrated that **GNR-SNO@MMT** effectively activated the immune system and exerted antitumor effects.

To investigate the ability of **GNR-SNO@MMT** to influence the tumor microenvironment, we assessed the microvessel density and pericyte coverage (a measure of vascular maturation) via CD31 and NG2 immunostaining. As shown in Fig. 8A, the mean vascular density was not obviously different between the G1-G5 groups, but the **GNR-SNO@MMT+L** treated group (G6) had a more uniform vascular distribution in the tumor than the other groups did. In addition, it had a larger NG2⁺/CD31⁺ region, suggesting that **GNR-SNO@MMT+L** enhanced the pericyte coverage of tumor vessels, thereby ameliorating the maturation of tumor vascular system. The molecular mechanism behind may be related to the role of NO to increase levels of cyclic guanosine to regulates the diastolic function of vascular endothelial cells [42]. Owing to normalization of the tumor vasculature, treatment with **GNR-SNO@MMT+L** further alleviated hypoxia at the tumor site, and a significant decrease in HIF-1 α expression was observed.

The hypoxic TIME is closely related to the immunosuppressive environment, such as promoting the aggregation of regulatory T cells, polarizing TAMs into an immunosuppressive M2 type, increasing the level of immunosuppressive cytokines, etc [14]. Inspired by the above findings, the effects of **GNR-SNO@MMT+L** treatment on PD-L1 expression, the TAMs phenotype and cytokines were further investigated. As shown by the results of the immunohistochemical staining (Fig. 8A), PD-L1 expression in the **GNR-SNO@MMT+L** treatment group (G6) obviously decreased, which facilitated

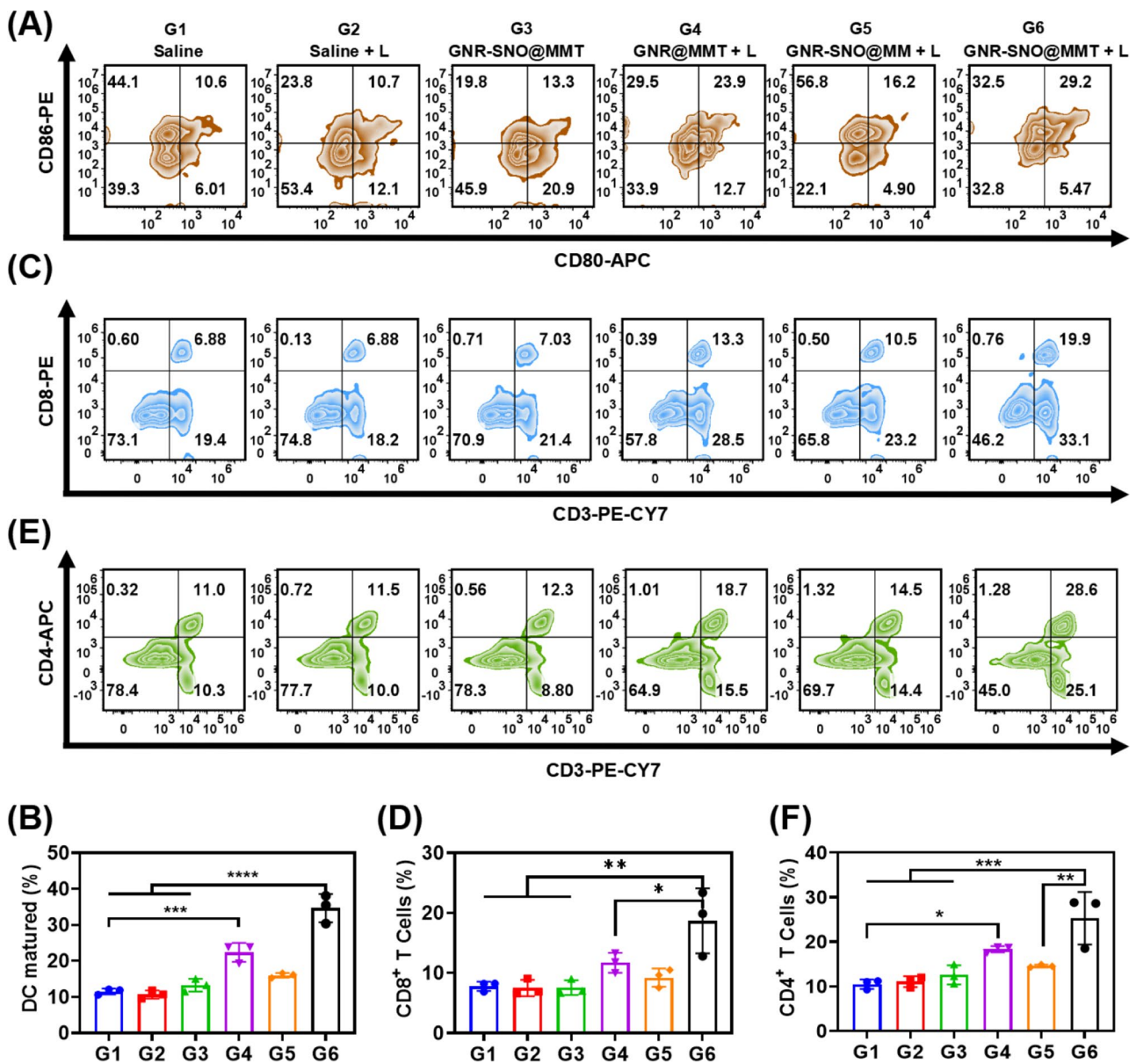


Fig. 7 In vivo TIME reconfiguration assessment. (A, B) DCs maturation of draining lymph nodes. (C, E) Flow cytometry and (D, F) frequency analysis of CD3⁺ CD8⁺ and CD3⁺ CD4⁺ T cells in the spleen

the anticancer capacity of the CTLs. Also, a distinct increase in the ratio of green (CD86⁺) M1 type TAMs/red (CD206⁺) M2 type TAMs was observed in tumor tissues, demonstrating that **GNR-SNO@MMT** together with laser irradiation repolarized TAMs to the immunostimulatory M1 type. In addition, the concentrations of inflammatory cytokines (TNF- α , IFN- γ , and IL-6) were significantly increased (Fig. 8B-E), and the NIR-II PTT and NO combination group (G6) owned the highest level. In contrast, the expression of the anti-inflammatory factor IL-10 was the lowest among all the groups. Taken together, **GNR-SNO@MMT** combined with NIR-II

irradiation not only activated anticancer immunity cascade but also comprehensively reprogrammed TIME.

Finally, we conducted a comprehensive analysis of the in vivo biocompatibility of **GNR-SNO@MMT**. Major organs, including the heart, spleen, and kidney were collected from the treated mice and subjected to H&E staining to assess any potential histological or pathological alterations. Encouragingly, our results showed no significant changes in these organs following the administration of **GNR-SNO@MMT** and subsequent NIR-II laser irradiation (Figure S4A). Furthermore, we assessed biochemical indices within the bloodstream of treated mice to gain insights into the systemic biocompatibility

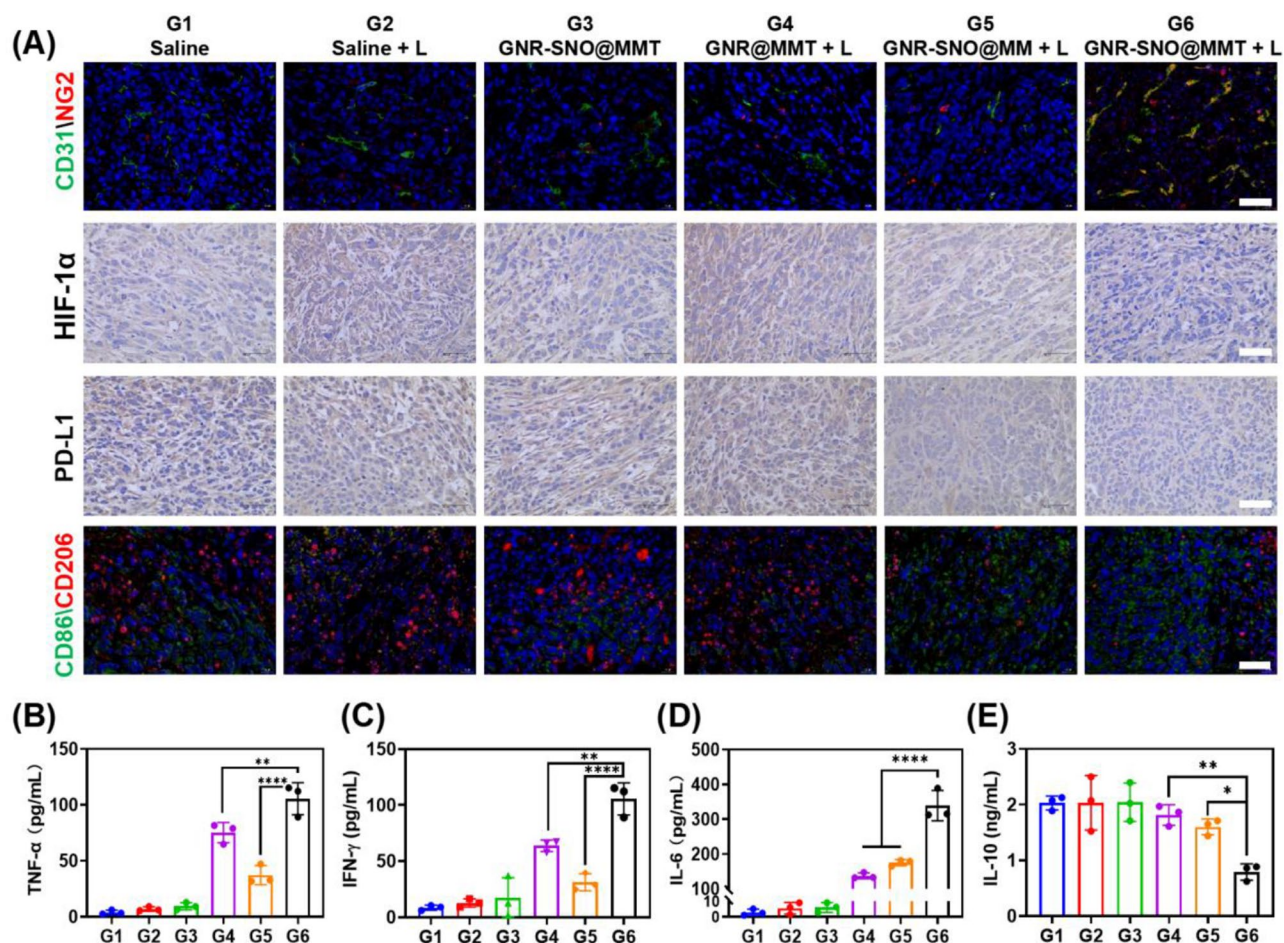


Fig. 8 (A) Immunohistochemical staining of intratumoral HIF-1 α and PD-L1 expression, immunofluorescence staining of CD31⁺ endothelial cells, NG2⁺ perivascular cells, CD86⁺ M1 type TAMs, and CD206⁺ M2 type TAMs (scale bar: 50 μ m). (B) TNF- α , (C) IFN- γ , (D) IL-6, and (E) IL-10 level in the serum by ELISA assay

of **GNR-SNO@MMT**. A panel of routine blood indices were analyzed, and all the parameters remained within physiologically normal ranges (Figure S4B). Notably, there were no significant differences in liver or kidney function indices (Figure S4C). These observations collectively implied that **GNR-SNO@MMT** exhibited a high degree of biocompatibility, with no discernible negative impact on the overall health of the mice.

Discussion

This study introduced a biomimetic gold nanomodulator, **GNR-SNO@MMT**, which employed a dual-pronged approach of NIR-II photothermal therapy and NO release to effectively normalize the tumor vascular system, alleviate hypoxia, and reprogram TIME in deep tumor. Compared with the reported systems (SI Table S1), our system owned several advantages. Firstly, **GNR-SNO@MMT** was design by grafting NO donors on the NIR-II PTAs of GNR, which is well known for its tunable and strong LSPR in the NIR region (Fig. 1D). This optical property was totally different and superior to the

organic PTAs [43]. So **GNR-SNO@MMT** had much better photothermal performance under irradiation of NIR-II (1064 nm) laser than NIR-I (808 nm) laser, which is favorable for deep tumor treatment (Fig. 2A-C). Meanwhile, NO release could be simultaneously effectively triggered by the photothermal effect. Therefore, the photosensitive platform **GNR-SNO@MMT** was flexible and controllable. Moreover, the biomimetic function of MM and tLyP-1 further endowed the whole system properties of the biocompatibility, long blood circulation, immune escape and specific tumor targeting and deep penetrating. This maybe a feasible way to guarantee the application of inorganic PTAs like GNR.

Secondly, both in vitro and in vivo results demonstrated that **GNR-SNO@MMT** generated substantial photothermal effects under NIR-II laser irradiation, leading to the tumors ablation and ICD induction (Figs. 4 and 7). This not only recruited CD8⁺ CTLs but also activated the immune system, providing synergistic enhancement of cancer immunotherapy. Furthermore, compared with the NIR-I laser, the use of NIR-II laser irradiation

presented considerable advantages because of its greater depth of tissue penetration and greater maximum permissible exposure, making it an optimal choice for treating deep-seated tumors.

Thirdly, NO, an endogenous signaling molecule with diverse roles in physiological and pathological processes, including the regulation of blood flow, immune responses, and apoptosis, plays crucial roles in our study. Our platform **GNR-SNO@MMT** is capable of reprogramming tumor microenvironment by NO and photothermal effect to reduce tumor interstitial fluid pressure, enhance blood perfusion, normalize the tumor vasculature at the tumor site (Fig. 5). Moreover, our findings confirmed that NO not only inhibits HIF-1 α expression in hypoxic tumor tissues but also disrupts the hypoxia-driven immunosuppression (PD-L1 & TAMs phenotype) (Fig. 8).

Despite these promising outcomes, our nanosystem still has room for improvement. Future work could focus on streamlining the complex synthesis process involved in the layer-by-layer modification and conjugation of -SNO side chains, which suffer from considerable loss and longer synthesis cycles. Moreover, combining our nanosystem with existing clinical immunological adjuvants or immune checkpoint inhibitors could enhance the immune response, leading to more effective photo-NO-immune therapy. By addressing these issues, we could work toward more efficient and clinically viable cancer treatments.

Conclusions

In summary, we successfully constructed a type of multifunctional biomimetic modulator **GNR-SNO@MMT** for the effective elimination of deep-sited tumors via robust NIR-II laser-activated PTT and NO gas modulation. The outer coat of the tLyp-1-engineered MM in **GNR-SNO@MMT** provided long circulation time, immune escape, tumor targeting and especially penetration into deeper regions of the tumor center. Upon NIR-II laser irradiation, the photothermal effect ablated tumors and induced effective ICD, activating the immune response. Moreover, NO gas molecules released in situ act as multifunctional immunomodulators, which not only normalized the tumor vascular system and alleviated hypoxia state but also comprehensively modulated TIME through the suppression of PD-L1, reprogramming TAMs phenotype and release of immunostimulatory cytokines. A robust photothermal immunotherapeutic effect was achieved via the biocompatible **GNR-SNO@MMT** together with NIR-II laser irradiation, which showed great promise for the treatment of deep-sited malignant tumors.

Abbreviations

NIR-II	Second near-infrared
TIME	Tumor immunosuppressive microenvironment

ICD	Immunogenic cell death
CTLs	Cytotoxic T lymphocytes
IFN- γ	Interferon- γ
PTAs	Photothermal agents
NIR-I	First near-infrared
LSPR	Localized surface plasmon resonance
GNR	Gold nanorods
TAMs	Tumor-associated macrophages
HIF-1 α	Hypoxia-inducible factor-1 α
PD-L1	Programmed cell death ligand-1
NO	Nitric oxide
SNO	S-nitrosothiols
MM	Macrophage membrane
tLyp-1	CGNKRTR (a tumor-homing penetrating peptide)
TNF- α	Tumor necrosis factor- α
IL-6	Interleukin-6
IL-10	Interleukin-10
BCA	Bicinchoninic acid
CCK-8	Cell Counting Kit-8
DIO	3,3'-diiodoacetylcarbocyanine perchlorate
CTAB	Hexadecyltrimethylammonium bromide
PVDF	Polyvinylidene fluoride
TEM	Transmission electron microscopy
EDS	Energy dispersive spectrometry
SDS-PAGE	Sodium dodecyl sulfate-polyacrylamide gel electrophoresis
CLSM	Confocal laser scanning microscopy
DAF-FM DA	Diaminofluorescein-FM diacetate
CRT	Calreticulin
HMGB-1	High-mobility group box 1
ELISA	Enzyme-linked immunosorbent assay
ICG	Indocyanine green
EPR	Enhanced permeability and retention
H&E	Hematoxylin and Eosin
TUNEL	Terminal-deoxynucleotidyl Transferase Mediated Nick End Labeling
DCs	Dendritic cells
PTT	Photothermal therapy
PBS	Phosphate buffered solution
ICP-MS	Inductively coupled plasma-mass spectrometry

Supplementary Information

The online version contains supplementary material available at <https://doi.org/10.1186/s12951-025-03304-2>.

Supplementary Material 1

Author contributions

Honglin Huang and Zhengxin Xie carried out the experiments, performed data analysis and wrote the manuscript. Yiyao Liu and Chunhui Wu critically revised the manuscript for important intellectual content. Li Zeng, Qianyi Zeng, Ziman Yang and Jinyang Shen assisted experiments. Ningxi Li, and Hong Yang participated in the program design. All authors read and approved the final manuscript and there are no conflicts to declare.

Funding

This research was supported, in whole or in part, by the National Natural Science Foundation of China (32171395, 52372263, 12132004, 32471367), the Sichuan Science and Technology Program (2024NSFSC0601, 2022NSFSC0048), and the Program for Innovative Fundamental Research Incubation of UESTC (Y03023206100226).

Data availability

No datasets were generated or analysed during the current study.

Declarations

Ethics and consent to participate

Female BALB/c mice were purchased from the Experimental Animal Center of Sichuan University (Chengdu, China). All the animal research was approved

by the Institutional Animal Care and Ethics Committee of the University of Electronic Science and Technology (approval number 1061420210305001).

Consent for publication

All the authors have read and approved the manuscript.

Competing interests

The authors declare no competing interests.

Author details

¹Sichuan Clinical Research Center for Cancer, Sichuan Cancer Hospital & Institute, Sichuan Cancer Center, and School of Life Science and Technology, University of Electronic Science and Technology of China, Chengdu, Sichuan 610041, P. R. China

²TCM Regulating Metabolic Diseases Key Laboratory of Sichuan Province, Hospital of Chengdu University of Traditional Chinese Medicine, No. 39 Shi-er-qiao Road, Chengdu, Sichuan 610072, P. R. China

³Department of Urology, Deyang People's Hospital, Deyang, Sichuan 618099, P. R. China

Received: 24 January 2025 / Accepted: 8 March 2025

Published online: 18 March 2025

References

- Mellman I, Chen DS, Powles T, Turley SJ. The cancer-immunity cycle: indication, genotype, and immunotype. *Immunity*. 2023;56(10):2188–205.
- Nam J, Son S, Park KS, Zou W, Shea LD, Moon JJ. Cancer nanomedicine for combination cancer immunotherapy. *Nat Rev Mater*. 2019;4(6):398–414.
- Galluzzi L, Guilbaud E, Schmidt D, Kroemer G, Marincola FM. Targeting immunogenic cell stress and death for cancer therapy. *Nat Rev Drug Discov*. 2024;23(6):445–60.
- Niu G, Song G, Kang Y, Zhai Y, Fan Y, Ye J, Li R, Li R, Zhang Y, Wang H et al. Quinoidal semiconductor nanoparticles for NIR-II photoacoustic imaging and photoimmunotherapy of cancer. *Adv Mater*. 2024;2415189.
- Huang H, Li N, Wei X, Li Q, Guo J, Yang G, Yang H, Cai L, Liu Y, Wu C. Biomimetic gemini nanoimmunoregulators orchestrated for boosted photoimmunotherapy by spatiotemporally modulating PD-L1 and tumor-associated macrophages. *Acta Pharm Sin B*. 2024;14(3):1345–61.
- Dong Y, Xia P, Xu X, Shen J, Ding Y, Jiang Y, Wang H, Xie X, Zhang X, Li W, et al. Targeted delivery of organic small-molecule photothermal materials with engineered extracellular vesicles for imaging-guided tumor photothermal therapy. *J Nanobiotechnol*. 2023;21(1):442.
- Cao YY, Li YL, Ren CX, Yang CK, Hao RZ, Mu TC. Manganese-based nanomaterials promote synergistic photo-immunotherapy: green synthesis, underlying mechanisms, and multiple applications. *J Mater Chem B*. 2024;12(17):4097–117.
- Wu C, Guan X, Xu J, Zhang Y, Liu Q, Tian Y, Li S, Qin X, Yang H, Liu Y. Highly efficient cascading synergy of cancer photo-immunotherapy enabled by engineered graphene quantum dots/photosensitizer/CpG oligonucleotides hybrid nanotheranostics. *Biomaterials*. 2019;205:106–19.
- Hong G, Antaris AL, Dai H. Near-infrared fluorophores for biomedical imaging. *Nat Biomed Eng*. 2017;1:0010.
- Sadr S, Hajjafari A, Rahdar A, Pandey S, Jafroodi PP, Lotfalizadeh N, Soroushi-anfar M, Kavasebi SS, Kharaba Z, Fathi-karkan S, et al. Gold nanobiosensors and machine learning: pioneering breakthroughs in precision breast cancer detection. *Eur J Med Chem Rep*. 2024;12:100238.
- Shi X, Ji Y, Hou S, Liu W, Zhang H, Wen T, Yan J, Song M, Hu Z, Wu X. Plasmon enhancement effect in Au gold nanorods@Cu₂O core-shell nanostructures and their use in probing defect States. *Langmuir*. 2015;31(4):1537–46.
- He T, Jiang C, He J, Zhang Y, He G, Wu J, Lin J, Zhou X, Huang P. Manganese-dioxide-coating-Instructional plasmonic modulation of gold nanorods for activatable duplex-imaging-guided NIR-II photothermal-chemodynamic therapy. *Adv Mater*. 2021;33(13):2008540.
- Saeed M, Chen F, Ye J, Shi Y, Lammers T, De Geest BG, Xu ZP, Yu H. From design to clinic: engineered nanobiomaterials for immune normalization therapy of cancer. *Adv Mater*. 2021;33(30):e2008094.
- Chen Z, Han F, Du Y, Shi H, Zhou W. Hypoxic microenvironment in cancer: molecular mechanisms and therapeutic interventions. *Signal Transduct Target Ther*. 2023;8(1):70.
- Binnewies M, Roberts EW, Kersten K, Chan V, Fearon DF, Merad M, Coussens LM, Gabrilovich DI, Ostrand-Rosenberg S, Hedrick CC, et al. Understanding the tumor immune microenvironment (TIME) for effective therapy. *Nat Med*. 2018;24(5):541–50.
- Barsoum IB, Smallwood CA, Siemens DR, Graham CH. A mechanism of hypoxia-mediated escape from adaptive immunity in cancer cells. *Cancer Res*. 2014;74(3):665–74.
- You L, Wu W, Wang X, Fang L, Adam V, Nepovimova E, Wu Q, Kuca K. The role of hypoxia-inducible factor 1 in tumor immune evasion. *Med Res Rev*. 2021;41(3):1622–43.
- Díaz-Bulnes P, Saiz ML, López-Larrea C, Rodríguez RM. Crosstalk between hypoxia and ER stress response: a key regulator of macrophage polarization. *Front Immunol*. 2020;10:2951.
- Liao C, Liu X, Zhang C, Zhang Q. Tumor hypoxia: from basic knowledge to therapeutic implications. *Semin Cancer Biol*. 2023;88:172–86.
- Liu P, Wang Y, Liu Y, Tan F, Li J, Li N. S-nitrosothiols loaded mini-sized Au@silica Nanorod elicits collagen depletion and mitochondrial damage in solid tumor treatment. *Theranostics*. 2020;10(15):6774–89.
- Xu Y, Liu J, Liu Z, Ren H, Yong J, Li W, Wang H, Yang Z, Wang Y, Chen G, et al. Blockade of platelets using tumor-specific NO-releasing nanoparticles prevents tumor metastasis and reverses tumor immunosuppression. *ACS Nano*. 2020;14(8):9780–95.
- Jiang W, Dong W, Li M, Guo Z, Wang Q, Liu Y, Bi Y, Zhou H, Wang Y. Nitric oxide induces immunogenic cell death and potentiates cancer immunotherapy. *ACS Nano*. 2022;16(3):3881–94.
- Kashiwagi S, Tsukada K, Xu L, Miyazaki J, Kozin SV, Tyrrell JA, Sessa WC, Gerweck LE, Jain RK, Fukumura D. Perivascular nitric oxide gradients normalize tumor vasculature. *Nat Med*. 2008;14(3):255–7.
- Theivendran S, Gu Z, Tang J, Yang Y, Song H, Yang Y, Zhang M, Cheng D, Yu C. Nanostructured organosilica nitric oxide donors intrinsically regulate macrophage polarization with antitumor effect. *ACS Nano*. 2022;16(7):10943–57.
- Kim J, Francis DM, Sestito LF, Archer PA, Manspeaker MP, O'Melia MJ, Thomas SN. Thermosensitive hydrogel releasing nitric oxide donor and anti-CTLA-4 micelles for anti-tumor immunotherapy. *Nat Commun*. 2022;13(1):1479.
- Yang Z, Gao D, Guo X, Jin L, Zheng J, Wang Y, Chen S, Zheng X, Zeng L, Guo M, et al. Fighting immune cold and reprogramming immunosuppressive tumor microenvironment with red blood cell membrane-camouflaged nanobullets. *ACS Nano*. 2020;14(12):17442–57.
- Chen L, Hong W, Ren W, Xu T, Qian Z, He Z. Recent progress in targeted delivery vectors based on biomimetic nanoparticles. *Signal Transduct Target Ther*. 2021;6(1):225.
- Wang J, Pan H, Li J, Nie D, Zhuo Y, Lv Y, Wang N, Chen H, Guo S, Gan Y, et al. Cell membrane-coated mesoporous silica nanorods overcome sequential drug delivery barriers against colorectal cancer. *Chin Chem Lett*. 2023;34(6):107828.
- Zhao H, Li L, Zhang J, Zheng C, Ding K, Xiao H, Wang L, Zhang Z. C-C chemokine ligand 2 (CCL2) recruits macrophage-membrane-camouflaged hollow bismuth selenide nanoparticles to facilitate photothermal sensitivity and inhibit lung metastasis of breast cancer. *ACS Appl Mater Interfaces*. 2018;10(37):31124–35.
- Cao H, Dan Z, He X, Zhang Z, Yu H, Yin Q, Li Y. Liposomes coated with isolated macrophage membrane can target lung metastasis of breast cancer. *ACS Nano*. 2016;10(8):7738–48.
- Ruoslahti E. Peptides as targeting elements and tissue penetration devices for nanoparticles. *Adv Mater*. 2012;24(28):3747–56.
- Teesalu T, Sugahara KN, Kotamraju VR, Ruoslahti E. C-end rule peptides mediate neuropilin-1-dependent cell, vascular, and tissue penetration. *PNAS*. 2009;106(38):16157–62.
- Wu C, Zhang Y, Wei X, Li N, Huang H, Xie Z, Zhang H, Yang G, Li M, Li T, et al. Tumor homing-penetrating and nanoenzyme-augmented 2D phototheranostics against hypoxic solid tumors. *Acta Biomater*. 2022;150:391–401.
- Song J, Yang X, Jacobson O, Huang P, Sun X, Lin L, Yan X, Niu G, Ma Q, Chen X. Ultrasmall gold nanorod vesicles with enhanced tumor accumulation and fast excretion from the body for cancer therapy. *Adv Mater*. 2015;27(33):4910–7.
- Mo R, Gu Z. Tumor microenvironment and intracellular signal-activated nanomaterials for anticancer drug delivery. *Mater Today*. 2016;19(5):274–83.
- Lu J, Liu X, Liao YP, Salazar F, Sun B, Jiang W, Chang CH, Jiang J, Wang X, Wu AM, et al. Nano-enabled pancreas cancer immunotherapy using immunogenic cell death and reversing immunosuppression. *Nat Commun*. 2017;8(1):1811.

37. Huang L, Li Y, Du Y, Zhang Y, Wang X, Ding Y, Yang X, Meng F, Tu J, Luo L, et al. Mild photothermal therapy potentiates anti-PD-L1 treatment for immunologically cold tumors via an all-in-one and all-in-control strategy. *Nat Commun.* 2019;10(1):4871.
38. Barsoum IB, Hamilton TK, Li X, Cotechini T, Miles EA, Siemens DR, Graham CH. Hypoxia induces escape from innate immunity in cancer cells via increased expression of ADAM10: role of nitric oxide. *Cancer Res.* 2011;71(24):7433–41.
39. Kwon J, Aoki Y, Takahashi H, Nakata R, Kawarasaki S, Ni Z, Yu R, Inoue H, Inoue K, Kawada T, et al. Inflammation-induced nitric oxide suppresses PPAR α expression and function via downregulation of Sp1 transcriptional activity in adipocytes. *Biochim Biophys Acta.* 2023;1866(4):194987.
40. Yan H, Shao D, Lao YH, Li M, Hu H, Leong KW. Engineering cell membrane-based nanotherapeutics to target inflammation. *Adv Sci.* 2019;6(15):1900605.
41. Sung YC, Jin PR, Chu LA, Hsu FF, Wang MR, Chang CC, Chiou SJ, Qiu JT, Gao DY, Lin CC, et al. Delivery of nitric oxide with a nanocarrier promotes tumour vessel normalization and potentiates anti-cancer therapies. *Nat Nanotechnol.* 2019;14(12):1160–9.
42. Carlström M, Weitzberg E, Lundberg JO. Nitric oxide signaling and regulation in the cardiovascular system: recent advances. *Pharmacol Rev.* 2024;76(6):1038–62.
43. Hao H, Yu M, Yi Y, Sun S, Huang X, Huang C, Liu Y, Huang W, Wang J, Zhao J, et al. Mesoporous calcium peroxide-ignited NO generation for amplifying photothermal immunotherapy of breast cancer. *Chem Eng J.* 2022;437:135371.

Publisher's note

Springer Nature remains neutral with regard to jurisdictional claims in published maps and institutional affiliations.